Journal of
Materials Chemistry A

ROYAL SOCIETY OF CHEMISTRY

PAPER

View Article Online
View Journal | View Issue

Cite this: *J. Mater. Chem. A*, 2025, **13**, 32741

Advanced characterization and functional evaluation of Ni-/Fe-doped Cu–Mn spinels as Co-free coatings for SOFC/SOEC interconnects

Łukasz Mazur, *[a] Kamil Domaradzki,[a] Paweł Winiarski,[a] Maciej Bik,[a] Andrzej Mikuła,[a] Juliusz Dąbrowa,[a] Grzegorz Cempura,[b] Anna Adamczyk,[a] Adam Kruk[b] and Tomasz Brylewski[a]

Received 22nd May 2025
Accepted 7th August 2025

DOI: 10.1039/d5ta04138d

rsc.li/materials-a

To develop Co-free, high-performance coatings for SOEC/SOFC interconnects, Ni- and Fe-doped $Cu_{1.3}Mn_{1.7}O_4$ spinels were synthesized *via* an EDTA-assisted gel method and applied onto low-chromium ferritic steel *via* electrophoretic deposition. Ni^{2+} preferentially substitutes Cu^{2+} in octahedral positions, increasing lattice parameters and improving electrical conductivity and corrosion resistance, while doping with Fe introduces structural disorder and secondary phases. DFT calculations confirm Ni and Fe's preference for octahedral Cu sites, aligning with experimental XRD, IR, and XAS analyses. Ni-doped spinels, particularly $CuMn_{1.7}Ni_{0.3}O_4$, exhibit enhanced conductivity and thermal stability, and are therefore promising materials for SOEC/SOFC applications. Reactivity studies show reduced Cr_2O_3 interaction, with CuO segregation observed for 0.1 mol dopants. Long-term oxidation tests demonstrate excellent corrosion resistance and stable ASR values in the 14–20 mΩ cm^2 range after 3000 hours at 750 °C, with Ni-doped coatings performing best. Confocal Raman imaging further revealed structural variations and phase distribution within the coating layers, and TEM studies demonstrated the complexity of the coating/steel interface, including the formation of a nanocrystalline Cr_2O_3 interlayer and progressive chromium diffusion into the spinel lattice. These features suggest a chemically graded, yet structurally coherent interface contributing to long-term coating stability. These findings highlight Ni doping as an effective strategy for optimizing CM spinel coatings for high-temperature electrochemical applications.

1. Introduction

In recent years, there has been growing interest in developing protective–conductive coatings for ferritic steel interconnects used in solid oxide fuel cells (SOFCs) and solid oxide electrolyzer cells (SOECs). Steel interconnects in SOFC/SOEC stacks are among the main components responsible for performance degradation due to oxidation and chromium volatilization, which reduce stack efficiency over time.[1–3] The coatings play a crucial role in mitigating chromium volatilization while ensuring long-term electrical and structural stability under harsh operating conditions. Spinel-structured oxides have emerged as highly promising materials for this purpose due to their ability to block Cr migration and maintain low area-specific resistance (ASR) across the steel/coating over thousands of hours, which is essential, as even small increases in ASR can significantly impact the power output and thermal management of a stack.[4–8]

Spinels exhibit a flexible crystal structure, with divalent cations typically occupying tetrahedral sites and trivalent or tetravalent cations residing in octahedral positions. This cation distribution enables property tuning through selective doping strategies.[9,10] Mn–Co-based systems are among the most studied spinels, offering high electrical conductivity (35–60 S cm^{-1}) and thermal expansion compatibility with ferritic steels.[11–17] However, due to cobalt's limited availability, rising cost, and toxicity, attention has shifted toward cobalt-free alternatives such as Ni–Fe, Cu–Fe, and Cu–Mn spinels.[18–22]

Within this group, Cu–Mn spinels (notably $Cu_{1.3}Mn_{1.7}O_4$) are distinguished by their excellent electrical conductivity and favorable thermal expansion coefficient, making them suitable candidates for interconnect coatings.[23–29] Despite these advantages, their high reactivity with Cr_2O_3 and long-term structural instability have hindered practical application. Earlier studies have shown that Cr diffusion leads to the formation of poorly conducting Cr-rich spinels, degrading electrical performance over time.[26]

---

[a] AGH University of Krakow, Faculty of Materials Science and Ceramics, Av. Mickiewicza 30, 30-059 Krakow, Poland. E-mail: lmazur@agh.edu.pl; Fax: +48 12 12 617 46 41; Tel: +48 12 617 46 41

[b] AGH University of Krakow, Faculty of Metals Engineering and Industrial Computer Science, Av. Mickiewicza 30, 30-059 Kraków, Poland

This study builds upon these challenges by exploring targeted doping with Ni and Fe as a strategy to enhance the functional properties of Cu–Mn spinels. While previous work has shown that Ni can stabilize the spinel phase and suppress Cr diffusion,[30–32] and Fe may influence electrical and structural behavior,[28] there are still few comprehensive studies combining both advanced material characterization and long-term functional evaluation.

The present research addresses this gap by systematically investigating the effects of Ni and Fe doping ($x = 0.1$ and 0.3) on the structural, electrical, and chemical behavior of $Cu_{1.3}Mn_{1.7}O_4$ spinels synthesized *via* a sol–gel route. A key novelty of this work lies in the combined application of advanced techniques – including X-ray absorption spectroscopy (XAS), density functional theory (DFT), confocal Raman imaging, and high-resolution TEM – to provide an in-depth understanding of the material's structure, cation distribution, and oxidation state dynamics, and their impact on high-temperature electrical performance.

Beyond fundamental characterization, the doped spinels are also evaluated as coatings applied *via* electrophoretic deposition on ferritic steel substrates. Their long-term oxidation behavior (3000 h at 750 °C), Cr-blocking performance, and ASR stability are examined under conditions relevant to SOEC/SOFC operation. By correlating intrinsic material properties with coating performance, this work offers a deeper insight into the design of cobalt-free spinel coatings and contributes to the development of durable, cost-effective solutions for next-generation electrochemical energy devices.

2. Experimental section

2.1. Preparation of powder materials

$Cu_{1.3}Mn_{1.7}O_4$ spinel (CM) powders were synthesized by means of wet chemistry methods, using the following substrates: copper nitrate ($Cu(NO_3)_2 \cdot 3H_2O$, p.a. Sigma-Aldrich, 99.999%), manganese nitrate ($Mn(NO_3)_2 \cdot 4H_2O$, p.a. Sigma-Aldrich, ≥97%), ethylenediaminetetraacetic acid (EDTA, $C_{10}H_{16}N_2O_8$, ALDRICH, 99.995%), citric acid ($C_6H_8O_7$, p.a. POCH), nickel nitrate ($Ni(NO_3)_2 \cdot 6H_2O$, p.a. Sigma-Aldrich, ≥97%), iron nitrate ($Fe(NO_3)_2 \cdot 9H_2O$, p.a. Sigma-Aldrich, 99.999).

Cu–Mn–(Ni/Fe)–O spinel powders were synthesized *via* EDTA gel processes. Copper, manganese, nickel, and iron cations were dissolved in deionized water, followed by the addition of EDTA (1.1 : 1 molar ratio) and pH adjustment to ∼8 using ammonia. The gel precursor was formed through heating and then pyrolyzed in a quartz crucible. Calcination at 750 °C for 5 h produced doped or undoped $Cu_{1.3}Mn_{1.7}O_4$ spinel powder.

High-energy milling was performed for 30 min in an YSZ vial with isopropanol (10 : 1 ball-to-powder ratio) using a SPEX 8000 Mixer/Mill. For electrophoretic deposition, the powders were milled for an extended time of 30 h in a PM100 (Retsh) ball mill with a Teflon chamber, isopropanol, and zirconium balls (1 : 2 : 1 volume ratio of powder : isopropanol : zirconium balls of 2 mm diameter). The powders were then dried and heated at 550 °C for 4 h to remove impurities.

2.2. Spinel sinter preparation

The $Cu_{1.3}Mn_{1.7}O_4$ (CM), $Cu_{1.2}Mn_{1.7}Ni_{0.1}O_4$ (CM01Ni), $CuMn_{1.7}Ni_{0.3}O_4$ (CM03Ni), $Cu_{1.2}Mn_{1.7}Fe_{0.1}O_4$ (CM01Fe), and $CuMn_{1.7}Fe_{0.3}O_4$ (CM03Fe) spinel powders were used to produce green bodies.

The milled powders were granulated in an agate mortar using two drops of a 2% polyvinyl alcohol solution per 0.5 g of powder. The coarse powder was uniaxially pressed at 50 MPa into ∼0.5 g cylindrical pellets with a diameter of 10 mm. The thermal treatment conditions were then optimized taking into account the structural stability of copper–manganese spinels within a narrow composition and temperature range.[33] The optimal sintering process conditions were determined to be 950 °C, 2 h in air, with heating and cooling rates of ∼6.5 °C min^{-1}.

2.3. Preparation of ferritic steel samples and cross-sections

Low-chromium Nirosta 4016/1.4016 ferritic steel (ThyssenKrupp VDM GmbH, Germany) was used as the metallic substrate for electrophoretic deposition. Its composition was as follows (wt%): Fe (balance), Cr – 16.2, C – 0.05, N – 0.04, Mn – 0.34, Si – 0.35, and P – 0.02.[34]

Steel samples (20 × 10 × 1 mm) were polished with SiC paper (1000–2000 grit), and 2 mm holes were drilled at the top. Before deposition, the substrates were ultrasonically cleaned in acetone for 2 min.

For microscopic analysis, the samples were cross-sectioned using an automatic cutter or fractured – for sintered specimens. They were embedded in a Struers EpoFix resin under vacuum and prepared with a Struers Tegramin-25 polisher. Grinding involved three 5-min steps on an MD Piano 220 with forces of 15, 10, and 5 N. Polishing was performed using MD Largo, MD Dac, and MD Dur cloths with DiaPro Allegro 9, DiaPro Dur 3, and DiaPro Dur 1 suspensions under the same conditions.

2.4. Electrophoretic deposition of the coatings

The Nirosta 4016/1.4016 steel samples were coated with spinels *via* electrophoretic deposition. The optimal solvent ratio (75 : 25 acetone/ethanol) and iodine concentration (2.0 g L^{-1}) were determined through rheological and electrophoretic testing.[35] The final suspension contained Cu–Mn–Ni/Fe powders (10 g L^{-1}), and it was sonicated for 10 min and aged for 2 h before deposition.

The EPD process used an S-LS-59 DC power supply (60 V, 5 A) with the following parameters: 60 V of voltage, an electrode distance of 7.5 mm, and 60 s of deposition time. After drying the samples at room temperature for 24 h, thermal treatment was performed in two steps: 8 h in Ar + 10% H_2 at 1000 °C, followed by 6 h in air at 850 °C, with a heating rate of ∼2.2 °C min^{-1}.

2.5. Structural/chemical composition studies and microscopic observations

The phase composition of all tested samples, *i.e.* sinters and oxidation products of clean steel and surface modified steel, was determined *via* X-ray diffraction (XRD). The X'Pert Pro PW

3710 diffractometer from Panalytical was used for these tests, with monochromatic CuKα radiation. The HighScore Plus (version 3.0.4) computer software was used in conjunction with the standard PCPDFWIN v.2.3 database to identify the phase composition of the tested samples. To determine the mass fractions and lattice parameters of the identified phases, the XRD data were analyzed using the Rietveld method, also utilizing aforementioned HighScore Plus software.

A Bruker Vertex 70v spectrometer was employed to conduct Fourier Transform Infrared (FTIR) spectroscopic studies in the mid-infrared (MIR) and far-infrared (FIR) regions under vacuum conditions. The transmission technique was used, which required preparing pellet-shaped samples. This was achieved by mixing approximately 1.5 mg of the powdered sample with 350 mg of KBr (Uvasol®, Merck) for the MIR region and approximately 3 mg of the sample with 180 mg of PE (Uvasol®, Merck) for the FIR region, followed by pressing them using an oil press. Pure pellets of KBr and PE materials were used as blanks for the MIR and FIR regions, respectively. A total of 256 and 512 scans at a resolution of 2 cm^{-1} were performed over the ranges of 4000–400 cm^{-1} for MIR and 400–100 cm^{-1} for FIR, respectively. The OPUS 7.2 software was used to acquire data and process the obtained spectra. The MIR spectra were analyzed in the 700–400 cm^{-1} range due to the absence of significant bands outside this range. The positions of individual bands were determined using the "peak picking" method.

To determine the oxidation states of transition metals in the studied samples, X-ray Absorption Near Edge Structure (XANES) spectroscopy – a variant of X-ray absorption spectroscopy – was employed. The L_3-edge XANES method reflects the transition of electrons from the $2p_{3/2}$ ground state to the unoccupied 3d state. Measurements were conducted at the 04BM PIRX beamline of the National Synchrotron Radiation Centre SOLARIS. The PIRX beamline utilizes a bending magnet (1.31 T) to generate photons with energies ranging from 100 to 2000 eV, with a resolution of 2.5×10^{-4} eV.[36] The samples were prepared using an Omicron sample holder with a carbon tape placed on top. The dimensions of the area exposed to the beam were 250 × 40 mm (horizontal × vertical). For Mn, Cu, Ni, and Fe metals, L_2 and L3 edge spectra were recorded in the total electron yield (TEY) detection mode. These measurements were performed at room temperature under ultra-high vacuum (UHV) conditions.

The obtained data were processed using the Bessy software. This involved normalizing the data to the incident photon flux (I_o), followed by subtracting a straight line fit to the pre-edge region of the L_3 edge and dividing the result by a polynomial function fitted to the post-edge region of the L_2 edge. The final step was the normalization of the intensity to a maximum value of 1.

Microscopic observations of the studied samples, including the fracture surfaces of sintered materials and the cross-sectional surfaces of steel/scale and steel/coating layered systems, were carried out using scanning electron microscopy (SEM). Observations for some of the samples were performed using a Thermo Fisher Scientific Phenom XL benchtop SEM equipped with an integrated energy-dispersive X-ray spectroscopy (EDS) microanalyzer. Observations for the remaining samples were carried out using a Thermo Scientific Apreo 2 SEM (Thermo Fisher Scientific) with an integrated EDS spectrometer. The porosity of the sintered materials was determined based on the SEM micrographs using the Porometric dedicated software (Thermo Fisher). For each sample, 25 SEM micrographs of different areas of the sintered materials were taken with a field of view of 89.5 μm. The final porosity was determined based on the average porosities computed for the 25 analyzed areas. The sample for electron microscopy was prepared using the FIB-SEM technique with a Zeiss Crossbeam 350 system. Two lamellae were prepared: the first, over 100 nm thick, was intended for EDS analysis and mounted on a molybdenum holder to reduce copper interference. The second, thinner lamella (under 100 nm), was mounted on a copper holder for high-resolution imaging.

A transmision electron microscopy (TEM) study was performed using an FEI Titan Cubed G2 60-300 TEM equipped with an FEG source, spherical aberration corrector, ChemiSTEM system, and Gatan GIF Quantum 963 energy filter. The following techniques were used: STEM-BF, STEM-HAADF and STEM-EDS. STEM-BF provided crystallite contrast *via* diffraction effects; HAADF enabled atomic-scale imaging; STEM-EDS allowed nanoscale chemical analysis, though some uncertainty in Cu quantification may arise due to copper components in the holder and microscope. EELS was employed for quantitative analysis, particularly of light elements.

A valuable addition to the physicochemical characterization of the investigated steel/coating systems is provided by Raman spectroscopy – more specifically, confocal Raman imaging. For this purpose, a WITec alpha300 M+ microscope equipped with a 488 nm solid-state laser, a ZEISS Epiplan-Neufluar objective (100×/0.9 NA), an UHTS 300 spectrometer, a 600 grooves per mm diffraction grating, an Andor CCD detector, and WITec control FIVE control software was used. The analyzed area varied depending on the sample type and coating thickness (constant width of 5 μm for coated samples and 20 μm for the unmodified steel sample), the acquisition time per spectrum was 8 s, and the sampling density was 0.5 μm. This area corresponded to the location on the cross-section plane observed *via* SEM microscopy and analyzed in terms of chemical composition using EDS. In total, between several hundred and over a thousand Raman spectra were obtained in the 60–1000 cm^{-1} range with a spectral resolution of 3.0 cm^{-1}. The obtained data were post-processed using the WITec project FIVE 5.3 PLUS software according to the standard protocol, including baseline correction (third-order polynomial) and noise removal (CRR filter). Subsequently, for characteristic spectral regions (*e.g.* the 555 cm^{-1} band for Cr_2O_3), an integration filter (with a specified position and bandwidth) was applied. This allowed chemical distribution maps to be generated; when these maps were superimposed, an image of the phase distribution is produced. The most representative spectra were extracted manually for each phase to determine the presence of predominant phases.

2.6. DFT calculations

Computational studies were performed using the Vienna *ab initio* simulation package (VASP),[37,38] while operating within the density functional theory (DFT) formalism. The structure relaxation was performed through a full optimization procedure, including spin-polarization mode, unit cell parameters, atomic sites, and ionic relaxation. The criteria used were: generalized gradient approximation (GGA), PBE[39] exchange–correlation potential, Monkhorst–Pack $4 \times 4 \times 4$ k-point mesh, 420 eV cut-off energy for plane wave basis sets, SCF (self-consisted field) energy convergence of 10^{-6} eV, ionic convergence of 2×10^{-2} eV A^{-1}. Due to the magnetic properties of elements, the initial magnetic moments were also included in the calculations with the following values: Fe – 3.0 μB, Mn – 3.5 μB, Cu – 2.2 μB, Ni – 2.0 μB.

The formation energy (per atom, E_{form}) of each material was evaluated using the total energy of the system, according to the enthalpy of creation approach (1):

$$E_{\text{form}} = \frac{E_{\text{tot,mat}} - \sum_{i=1}^{n} N_i \cdot E_{\text{tot,elem}}}{N_i}, \tag{1}$$

where $E_{\text{tot,mat}}$ – total energy of the system, N_i – number of atoms in the structure, $E_{\text{tot,elem}}$ – total energy of the Cu, Fe, Ni, Mn, and O subsystems (calculated separately for the most thermodynamically stable phases of each element).

The defect formation energy (E_{def}) was also estimated taking into consideration the substitutions of Ni/Fe → Cu/Mn, using the standard approach (2):

$$E_{\text{def}} = \frac{E_{\text{tot,def-mat}} - E_{\text{tot,undef-mat}} - n_{\text{s}} E_{\text{Ni/Fe}} + n_{\text{s}} \cdot E_{\text{S}}}{D_i}, \tag{2}$$

where $E_{\text{tot,def-mat}}$ – total energy of the defected system, $E_{\text{tot,undef-mat}}$ – total energy of the undefected system, $E_{\text{Ni/Fe}}$ – total energy of nickel or iron atom, n_{s} – number of substituted atoms, E_{S} – total energy of Cu/Mn atom, D_i – number of defects in the structure.

Structural analysis and visualization of the optimized model structures were performed using the VESTA software.[40] A simple, basic unit cell of the cubic $Fd\bar{3}m$ spinel was first calculated. Based on this basic spinel structure, a model in which two Mn ions were substituted with Cu, resulting in the nominal composition of $Cu_{1.25}Mn_{1.75}O_4$, was created. Based on the latter, optimized system, one or two selected ions were substituted with nickel or iron: in initial Cu sites in tetrahedral coordination (denoted as $Cu_{1.125}Ni_{0.125}Mn_{1.75}O_4$_A, $CuNi_{0.25}Mn_{1.75}O_4$_A, $Cu_{1.125}Fe_{0.125}Mn_{1.75}O_4$_A, $CuFe_{0.25}Mn_{1.75}O_4$_A), in initial Cu sites in octahedral coordination (denoted as $Cu_{1.125}Ni_{0.125}Mn_{1.75}O_4$_B, $CuNi_{0.25}Mn_{1.75}O_4$_B, $Cu_{1.125}Fe_{0.125}Mn_{1.75}O_4$_B, $CuFe_{0.25}Mn_{1.75}O_4$_B), or in initial Mn sites in octahedral coordination (denoted as $CuNi_{0.125}Mn_{1.625}O_4$_C, $CuNi_{0.25}Mn_{1.5}O_4$_C, $CuFe_{0.125}Mn_{1.625}O_4$_C, $CuFe_{0.25}Mn_{1.5}O_4$_C). Additionally, considering the energetic stability of the system and taking into account the potential presence of foreign phases (based on experimental data), analogous calculations were also performed for NiO ($Fm\bar{3}m$), CuO ($C2_1/c$), Fe_2O_3 ($R\bar{3}c$), and Mn_2O_3 ($Ia\bar{3}$) oxides, as well as the tetrahedral spinel ($I4_1/amd$) and cubic bixbyite structure ($Ia\bar{3}$) with varying Fe : Mn ratio: $FeMn_2O_4$, $Fe_{1.5}Mn_{1.5}O_4$, $FeMn_3O_6$, and $Fe_2Mn_2O_6$, respectively.

2.7. Resistivity measurements

Electrical conductivity and the Seebeck coefficient were measured using a two-probe four-point DC method over a 300–900 °C range. The setup included a TF1200 tube furnace, a Keysight 34465A multimeter, a Keysight 33210A waveform generator, a CFRASB-1000 control unit, a BR07 retaining decade, a SSC-15 measuring probe, and an AM16/32B multiplexer.

Rectangular specimens polished using 1000-grit SiC abrasive paper were used, with dimensions measured by means of a caliper. The samples were heated to 900 °C and cooled to 300 °C with electrical resistance recorded at 25 °C intervals. The estimated relative error in conductivity measurements was ∼5%. Electrical conductivity was calculated using the corresponding formula:

$$\sigma = \frac{L}{S \cdot R} \tag{3}$$

where: R – resistivity of the tested samples [Ω], S – area of the Pt electrodes [cm^2], L – thickness [cm]. The electrical conductivity values calculated for the spinel specimens were adjusted for porosity using Bruggeman's model, according to the following formula:[41]

$$\sigma = \sigma_{\text{m}} \cdot \frac{1}{(1-p)^{3/2}} \tag{4}$$

where: σ – conductivity after adjusting for porosity [S cm^{-1}], σ_{m} – measured conductivity [S cm^{-1}], p – sinter porosity [–].

Electrical conduction in all studied spinel samples was a thermally activated process. Consequently, the activation energies of electrical conduction for these samples were calculated by applying the Nernst–Einstein dependence:[28]

$$\ln(\sigma \cdot T) = \ln \sigma_0 - \frac{E_{\text{a}}}{k \cdot T} \tag{5}$$

where: σ – electrical conductivity [1 (Ω cm)$^{-1}$], σ_0 – pre-exponential factor [1 (Ω cm K)$^{-1}$], k – Boltzmann constant [eV K^{-1}], E_{a} – activation energy of electrical conduction [eV], and T – absolute temperature [K].

Area-specific resistance, a standard metric for measuring the electrical resistance of oxidized materials, was calculated for the studied systems by multiplying the resistance by the contact surface area of the oxide and steel. The samples were coated with platinum electrodes (8 mm in diameter) and heated to 750 °C for 15 minutes to remove organic binder residue, and then placed between platinum electrodes in a horizontal tube furnace. This symmetrical sample arrangement allowed the calculation of area-specific resistance using the equation:

$$\text{ASR} = \frac{R \cdot A}{2} \tag{6}$$

where R represents electrical resistance [Ω], and A denotes the surface area of the Pt contact layer [cm^2]. A two-probe four-point DC method was used to evaluate the oxidation products' electrical resistance. Measurements were taken while the samples cooled over the temperature range from 750 °C to 300 °C and at intervals of 50 °C.

2.8. Oxidation tests

The samples underwent quasi-isothermal oxidation tests over 3000 h in a laboratory air atmosphere at 750 °C; they were periodically removed from the furnace, cooled to approximately 300 °C, and allowed to reach ambient temperature before further analysis. Oxidation kinetics were determined by measuring mass gain after every 300-hour interval using a Radwag XA 210 analytical balance with a sensitivity of 10^{-5} g. The obtained oxidation kinetics curves of the tested samples allowed the parabolic oxidation rate constants to be estimated using the Pilling–Bedworth equation:[42]

$$\left(\frac{\Delta m}{A}\right)^2 = k_\mathrm{p}\cdot t + C \tag{7}$$

where: $\Delta m/A$ – mass gain per unit area [g cm^{-2}], k_p – parabolic rate constant [g^2 cm^{-4} s^{-1}], t – reaction time [s], and C – integration constant defining the onset of parabolic kinetics.

2.9. Reactivity tests with Cr_2O_3

To reach preliminary conclusions concerning the suitability of the studied materials for use in the production of protective–conductive coatings on steel interconnects, their reactivity in the form of sinters was tested by covering them with powdered chromium oxide. The CM, CM01Ni, CM03Ni, CM01Fe and CM03Fe sinters were selected for these tests. The samples were placed in a crucible filled with chromium oxide in the chamber furnace and, after 150 h of exposure to air at 800 °C, the depth of chromium penetration into the sinter was determined using linear EDS analysis.

3. Results

3.1. Structural studies

Phase analysis of calcinated powders (Fig. 1) revealed two phases in all samples except CM01Ni: a regular CM spinel ($Fd\bar{3}m$, ICDD 01-070-0262) and a bixbyite Mn_2O_3 phase ($Ia\bar{3}$, ICDD 00-041-1442). The CM03Fe sample contained the highest amount of the secondary phase with *ca.* 1/3 of the total mass (Table 1).

After sintering for 2 h in air at 950 °C, Mn_2O_3 peaks disappeared for all samples except the CM one, in which case the secondary phase remained unchanged. In CM03Fe, bixbyite transformed into a tetragonal spinel ($I4_1/amd$, ICDD 00-034-1322). The CM01Ni sample remained monophasic after both calcination and heat treatment. Table 1 presents lattice parameters and phase fractions of CM, CM01Ni, CM03Ni, CM01Fe, and CM03Fe sinters after calcination (750 °C, 5 h) and sintering (950 °C, 2 h), determined based on Rietveld analysis.

The lattice parameter of the regular spinel phase in sinters treated at 950 °C was higher than for powders calcinated at 750 °C. After calcination, all powders exhibited similar lattice parameters; however, in the sinters the dopants caused significant unit cell expansion. The greatest expansion was observed for CM01Fe and CM03Ni, while CM03Fe exhibited the smallest degree. Fig. S1 presents a zoomed-in view of the high-intensity peak near 36° for sintered spinels, visually confirming the peak shifts and the unit cell expansion.

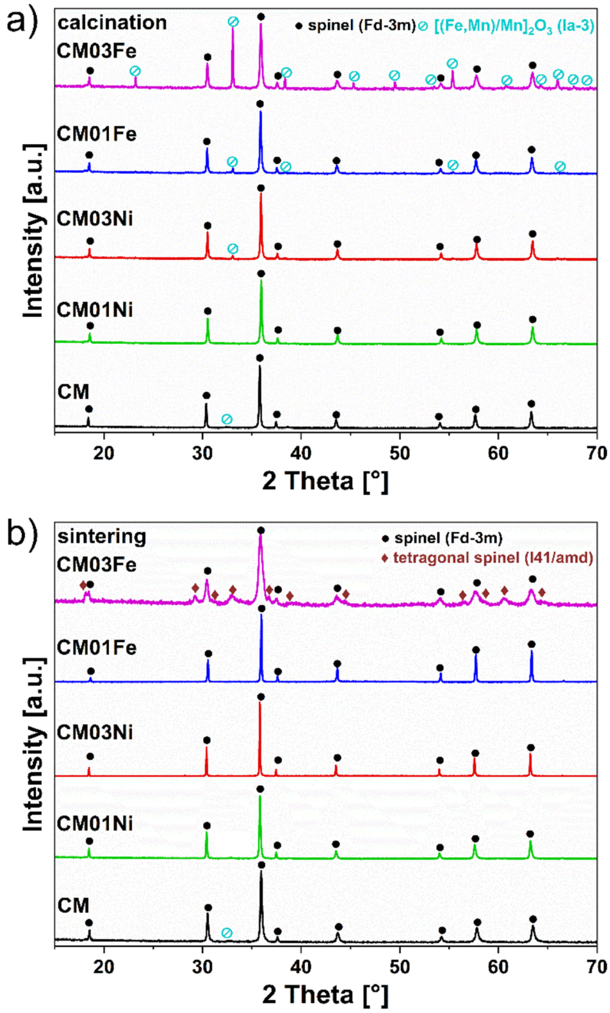

Fig. 1 X-ray diffraction patterns for (a) calcinated powders and (b) sinters of Ni and Fe CM doped spinels.

As opposed to the observations made by Ignaczak *et al.*,[28] *i.e.* that unit cell size decreases with increasing Fe content, Fe-doped spinels in the present study had comparable lattice parameters. Additionally, spinels with 0.1 and 0.3 mol Fe had similar phase compositions, forming either a single-phase regular spinel or a two-phase structure with tetragonal spinel.

To complement the structural studies performed using X-ray diffraction, X-ray absorption spectroscopy (XAS) and mid- and far-infrared (MIR and FIR) spectroscopy techniques were also added to the applied array of research techniques to enable a deeper analysis of the studied spinels' structure. Infrared spectroscopy allows the determination of subtle structural changes occurring in the CM spinel structure due to the substitution of Cu^{2+} cations in its unit cell by Ni^{2+} or Fe^{2+}/Fe^{3+} cations. These changes in the structure of regular spinel may be registered thanks to the presence of four active bands in the IR range, which, according to group theory, are assigned to the vibrations of octahedral units (ν_1 and ν_2 – mid-infrared range,

Table 1 Lattice parameters of the regular spinel phase and mass fractions of the detected phases in a series of sinters based on CM spinel

	Calcination (750 °C)			Sintering (950 °C)		
		Mass fraction of phases [%]			Mass fraction of phases [%]	
Sample	Lattice parameter a [Å]	$Fd\bar{3}m$	$Ia\bar{3}$	Lattice parameter a [Å]	$Fd\bar{3}m$	$Ia\bar{3}$ ($I4_1/amd^a$)
CM	8.2853(1)	99.0	1.0	8.2769(3)	98.9	1.1
CM01Ni	8.2891(2)	100	—	8.3072(2)	100	—
CM03Ni	8.2842(2)	95.8	4.2	8.3140(1)	100	—
CM01Fe	8.2875(2)	94.6	5.4	8.3162(2)	100	—
CM03Fe	8.2862(2)	66.2	33.8	8.2937(9)	60.2	39.8^a

[a] Tetragonal phase.

MIR) or mostly originate from both octahedral and tetrahedral units (ν_3) or tetrahedral units alone (ν_4) – both in the far-infrared range (FIR).[43,44] Fig. 2 visually combines the spectra in both the MIR and FIR ranges. Measurements were carried out for a series of spinel materials based on pure CM and doped with various amounts of Ni or Fe cations, obtained after 5 h of calcination at 750 °C (samples marked as "after calcination") and after an additional 2 h of heat treatment in air at 950 °C (samples marked as "after sintering").

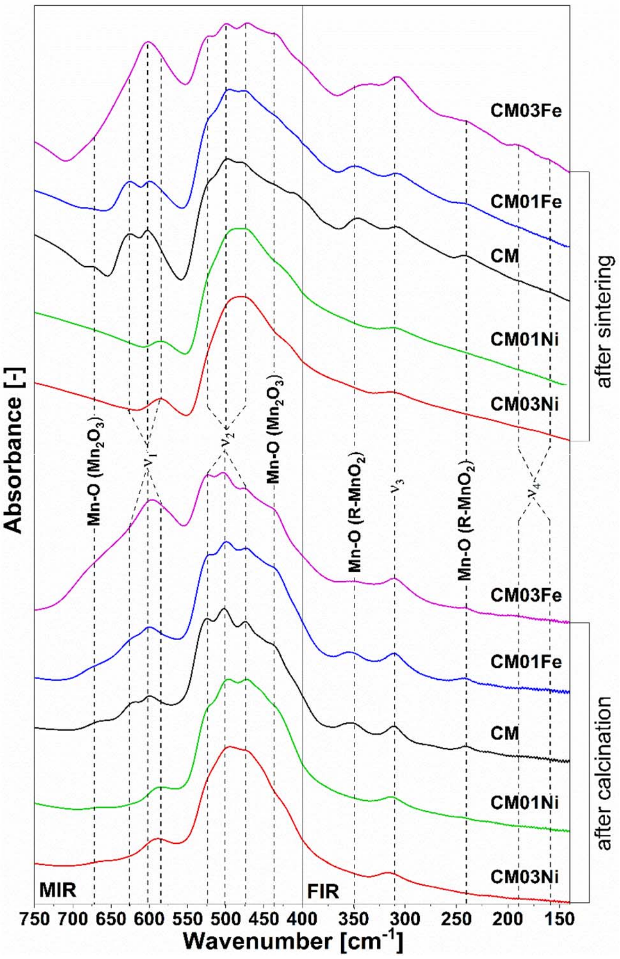

Fig. 2 Spectra recorded in the mid-infrared (MIR) and far-infrared (FIR) ranges for a series of CM01Ni, CM03Ni, CN01Fe and CM03Fe sinters after their calcination and sintering processes. The positions of spinel bands ν_1–ν_4 are marked on the spectra.

For pure CM spinel, the main absorption areas in the MIR range for both the calcinated and sintered samples can be assigned to active bands ν_1 and ν_2 typical to the spinel structure – at around 626, 602 and 575 cm^{-1} (ν_1) and around 524, 501, and 474 cm^{-1} (ν_2).[43,44] In the case of both bands, the triple degeneration results from the phenomenon of partial or complete inversion of the spinel structure, which is likely related to the non-stoichiometry of $Cu_{1.3}Mn_{1.7}O_4$ and copper's occupation not only of tetrahedral positions but also of thermodynamically unfavorable octahedral positions. Therefore, to satisfy the electronegativity condition, the octahedral positions must also contain Mn^{4+} ions in addition to Mn^{3+}. Furthermore, the remaining visible bands in the MIR region can be attributed to Mn–O bond vibrations in the bixbyite Mn_2O_3 structure,[45] which is consistent with the X-ray diffraction results, which indicated the presence of this phase. The main difference observed for this material after sintering compared to the calcinated sample is a decrease in the intensity of all three ν_2 bands for all compositions. Taking into account the fact that these bands occurred due to band triple degeneration, such observation can be described as the degeneration decrease, probably due to a partial structural ordering during the sintering process and final higher symmetry. This may mean that at this temperature both Cu^{2+} and Mn^{4+} thermodynamically unfavorable cations leave octahedral positions in the spinel structure. While this was not observable directly in the diffractograms of the studied sinters (Fig. 1), the noticeable increase in the lattice parameters of the regular spinel unit cell after sintering may be related to a smaller amount of Cu and Mn in its structure (Table 1). Moreover, no significant differences are observed in the spectra recorded for the calcinated and sintered samples. The only exception is the CM03Fe sample, whose phase composition before and after heat treatment differs, as evident from the corresponding MIR spectra. In the calcinated sample, the bands originating from the bixbyite Mn_2O_3 structure, clearly visible at around 672 and 437 cm^{-1}, disappear after the sintering process, which is consistent with the results of X-ray diffraction studies, with no peaks originating from this phase recorded for the CM03Fe sinter.

Differences in the FTIR spectra for pure CM spinel and CM spinel doped with Ni or Fe can be explained by the concept of cation "covalency", as proposed in.[46] Based on the calculated values of the *N*–*V* parameter, where *N* is the number of unpaired electrons and *V* is the valence state, the bond strength can be estimated, which can be different for Mn, Cu, Ni, and Fe. The higher the *N*–*V* value, the lower the covalency (in terms of "pulling" electron density from oxygen towards the metal cation) and thus the weaker the bond and ultimately the shift of bands towards lower wavenumbers in FTIR spectra.[47,48] For the studied materials, the individual *N*–*V* parameters can be calculated as follows: Cu^{2+}: $1 - 2 = -1$, Mn^{2+}: $5 - 2 = 3$, Mn^{3+}: $4 - 3 = 1$, Mn^{4+}: $3 - 4 = -1$, Ni^{2+}: $2 - 2 = 0$, Fe^{2+}: $4 - 2 = 2$ and Fe^{3+}: $5 - 3 = 2$. For samples containing Ni, the ν_1 band clearly shifted towards lower wavenumbers (*ca.* 20–30 cm^{-1}) and a change in the bands' contour was observed. Such observations may indicate that Ni^{2+} was located in octahedral positions in place of thermodynamically unfavorable Cu^{2+}, which manifested itself in the spectra in the form of ν_2 bands' degeneration decrease due to structural ordering. On the other hand, doping with Fe^{2+} and/or Fe^{3+} cations occurred in a different manner than in the case of Ni^{2+} cations. When comparing the spectra of pure CM spinel and CM spinel doped with iron cations, no visible changes in the positions of the ν_1 bands (as observed for Ni substitutions) can be seen – only for CM03Fe samples, the bands broadened significantly. On the other hand, for the ν_2 region, the bands (especially the one at around 524 cm^{-1}) shifted slightly – by *ca.* 4 cm^{-1} – towards lower wavenumbers only for the CM01Fe samples, which may have occurred due to the substitution of Cu^{2+} cations by Fe cations – most likely Fe^{2+}, which have a greater preference for occupying octahedral positions compared to Fe^{3+}.[49] At the same time, there was no visible change in ν_2 band degeneration. In turn, for CM03Fe samples, no shift was visible, but band degeneration increased, especially for the band at *ca.* 524 cm^{-1}. This was probably due to the increase in Cu^{2+} cation concentration as a result of tetragonal spinel formation, which decreased the sample symmetry. Additionally, the sintered CM03Fe sample exhibited a significant broadening of the bands compared to the remaining samples, which may also have been due to the presence of two spinel phases in the material, also observed in the XRD diffractogram for this material.

In the FIR range, two additional absorption areas were visible, corresponding to the ν_3 and ν_4 bands. In addition, there were also bands originating from Mn–O bonds in R–MnO_2.[45] The ν_3 band was located at around 310 cm^{-1} and was similar for all samples except the CM03Fe sinter, for which its intensity increased, most likely due to the presence of a phase with a tetragonal structure in addition to the regular spinel phase. Similarly, for the active ν_4 band, which strongly depends only on the mass of the cations in tetrahedral positions,[43] the effect of doping was noticeable only for the sintered CM03Fe sample. In Fig. 2, two broad bands of very low intensity can be seen at around 190 and 159 cm^{-1}, which suggests the presence of two types of cations in tetrahedral positions, *i.e.* lighter Mn^{2+} at a higher wavenumber and heavier Cu^{+} at a lower wavenumber.[43,44]

To determine the influence of Ni or Fe dopants on the valence state of transition metals in the structure of the investigated spinels, both the samples obtained *via* calcination alone and those that underwent additional sintering at a temperature of 950 °C for 2 h were studied using the XANES method with TEY detection. As reference samples, oxides with a stable valence state were used, which involved the analysis of the following cations: Cu^{+} in Cu_2O, Cu^{2+} in CuO, Mn^{2+} in MnO, Mn^{3+} in Mn_2O_3, Mn^{4+} in MnO_2, Fe^{3+} in Fe_3O_4, Ni^{2+} in NiO, and Ni^{3+} in $LaNi_{0.6}Fe_{0.4}O_3$, since Ni^{3+} cations are the only nickel cations present in this oxide.[50] All XANES spectra recorded for samples of pure CM spinel and CM spinels doped with various amounts of Ni or Fe are presented in Fig. 3.

The L_3-edge XANES spectra recorded for copper were characterized by a main peak at ~930.9 eV, corresponding to Cu^{2+} (Fig. 3a). It should be noted that this peak was shifted slightly compared to the peak originating from Cu^{2+} in CuO for all doped CM spinels after the calcination process, which may indicate the appearance of small amounts of Cu^{+}.[51] For all sintered samples, the peak corresponding to Cu^{2+} was located at the same position. However, for CM03Fe, an additional distinct peak was observed around 934 eV, indicating the presence of a significant amount of Cu^{+} cations in the sample, which was also confirmed by the results of FIR measurements (Fig. 2).

The largest differences in the XANES spectra of the studied samples were observed for the manganese L_3 edge, which exhibited a wide spectrum of manganese cation oxidation states (Fig. 3b). Importantly, doping the CM sample with nickel did not affect the valence state of manganese cations in the spinel structure, while doping with Fe clearly did. Such observations agree with the assumptions postulated based on the analysis of the IR spectroscopy results. The introduction of Fe into the structure in any studied amount lead to a decrease in the Mn^{4+}/Mn^{3+} cation ratio and in the case of the CM01Fe sample also an increased proportion of Mn^{2+}, which was noticeable for materials obtained after the calcination process. The observed tendencies resulted from changes in the intensity of the peaks at ~640.2 eV, ~642.3 eV, and ~643.5 eV, corresponding to Mn^{2+} in MnO, Mn^{3+} in Mn_2O_3, and Mn^{4+} in MnO_2, respectively. On the other hand, the sintering process of CM01Fe caused the peak corresponding to Mn^{4+} for this sample to remain unchanged compared to the pure CM spinel, while for the CM03Fe sample the proportion of Mn^{2+} increased, most likely due to the presence of tetragonal spinel, which was also confirmed by IR studies.

The L_3-edge XANES spectra for nickel (Fig. 3c) and iron (Fig. 3d) did not differ significantly for materials obtained after calcination and those after additional sintering. The Ni L_3 spectra for CM samples were characterized by the presence of only one peak at ~853.2 eV, which corresponds to Ni^{2+} in NiO. On the other hand, the XANES spectra of the iron L_3 edge correspond to a typical spectrum for Fe_3O_4, which means that in these materials, Fe assumes both +2 and +3 oxidation states.

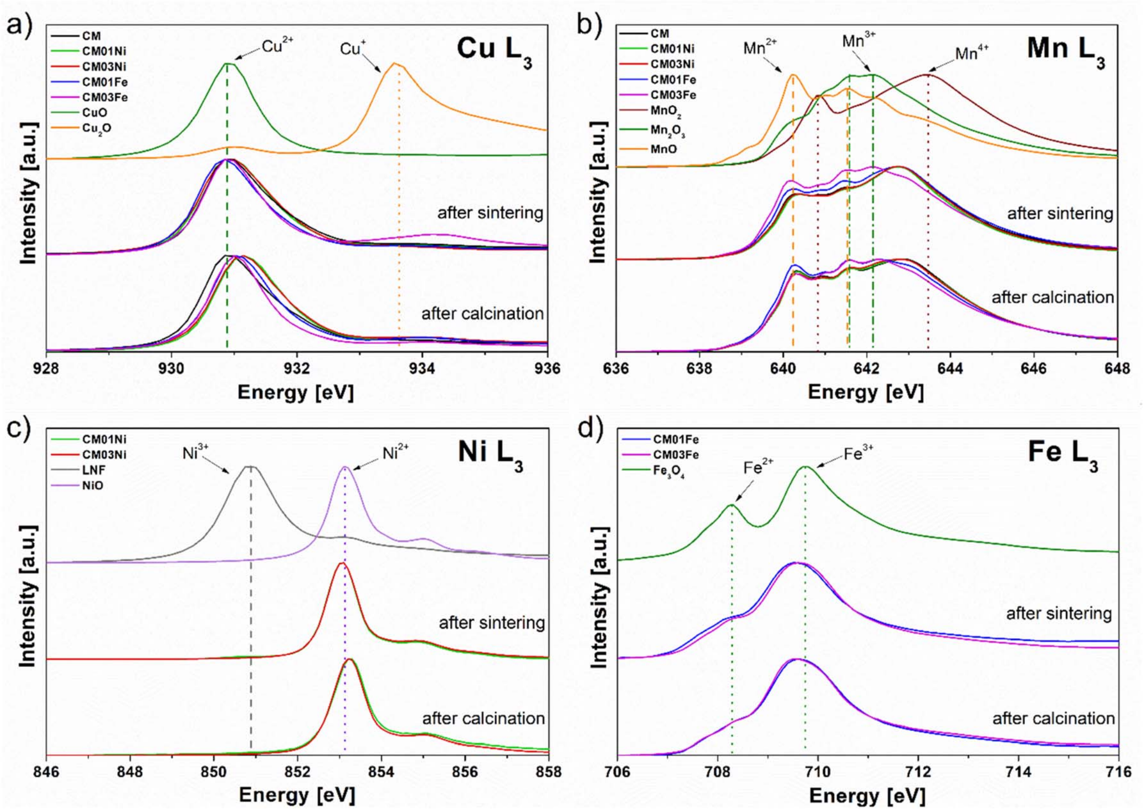

Fig. 3 X-ray absorption near-edge structure (XANES) spectra at the L_3 edge for: (a) copper, (b) manganese, (c) nickel, and (d) iron, recorded for CM, CM01Ni, CM03Ni, CM01Fe, and CM03Fe samples, and also for selected reference materials.

3.2. Prediction of Ni or Fe dopant substitutions in the $Cu_{1.3}Mn_{1.7}O_4$ spinel structure based on DFT calculations

Fig. 4a shows the formation energies of spinels based on CM doped with Ni or Fe in molar amounts of 0.125 and 0.25, considering three variants of substitutions: for copper in the tetrahedral (A) or octahedral (B) position and for manganese in the octahedral position (C). In addition, the formation energy (E_{form}) of various oxides that can form secondary phases in the studied materials is also shown. Fig. 4b shows the formation energy of defects (E_{def}) for Ni or Fe dopants located in appropriate positions of the spinel structure.

All studied systems exhibited negative E_{form} values (Fig. 4a). The most energetically favorable structure in the case of doping with either Ni or Fe was determined to be one in which they substitute copper in octahedral sites. The same conclusions can be drawn by analyzing E_{def} (Fig. 4b). It is less likely that nickel and iron will occupy tetrahedral positions, while a system in which they substitute manganese in octahedral sites would be entirely unfavorable. Taking into account the experimental data, it appears that nickel indeed incorporates into these structures over a wide range of concentrations. On the other hand, the presence of iron results in the precipitation of the tetrahedral form of manganese–iron spinel or regular bixbyite phase. Such an arrangement seems justified when analyzing the resultant formation energy of the individual components. Considering separate oxides, the most thermodynamically stable compound is the Mn_2O_3 manganese oxide. Since it combines manganese with copper, the $Cu_{1.25}Mn_{1.75}O_4$ spinel is definitely more desirable than a mixture of CuO and Mn_2O_3 oxides (Fig. 4a). Incorporating nickel into this structure seems energetically favorable compared to the precipitation of spinel and nickel oxide or a mixture of individual oxides (particularly when Ni is located in initial Cu octahedral sites, version B). In the case of iron, the opposite is true. When adding iron to $Cu_{1.25}Mn_{1.75}O_4$, the resultant formation energy values suggest the stability of both the tetragonal spinel and bixbyite phases. Moreover, the combination of these two binary oxides and $Cu_{1.25}Mn_{1.75}O_4$ is more energetically favorable than the Fe-doped system or the mixture of individual oxides. This is consistent with the experimental results, which suggest a very limited range of iron solubility in $Cu_{1.25}Mn_{1.75}O_4$ spinel.

Considering the experimental results, it can also be observed that successful doping with nickel should result in increased lattice parameters (Fig. 4c). Although nickel polyhedra are smaller than copper ones, they influence the elongation of Cu–O and Mn–O bonds in the remaining positions regardless of the position they themselves occupy (which is related to the level of distortion and local structure deformation, see SI. Table S1), leading to the swelling of the unit cell (Fig. 4d and Table S1). This effect is only disrupted for low concentrations of the Ni dopant in version B due to the smaller dimensions of the nickel polyhedra and minor deformation in this model structure. The reduction in the size of MnO_6 polyhedra is evident when Ni substitutes Mn in this sublattice, but since this substitution is

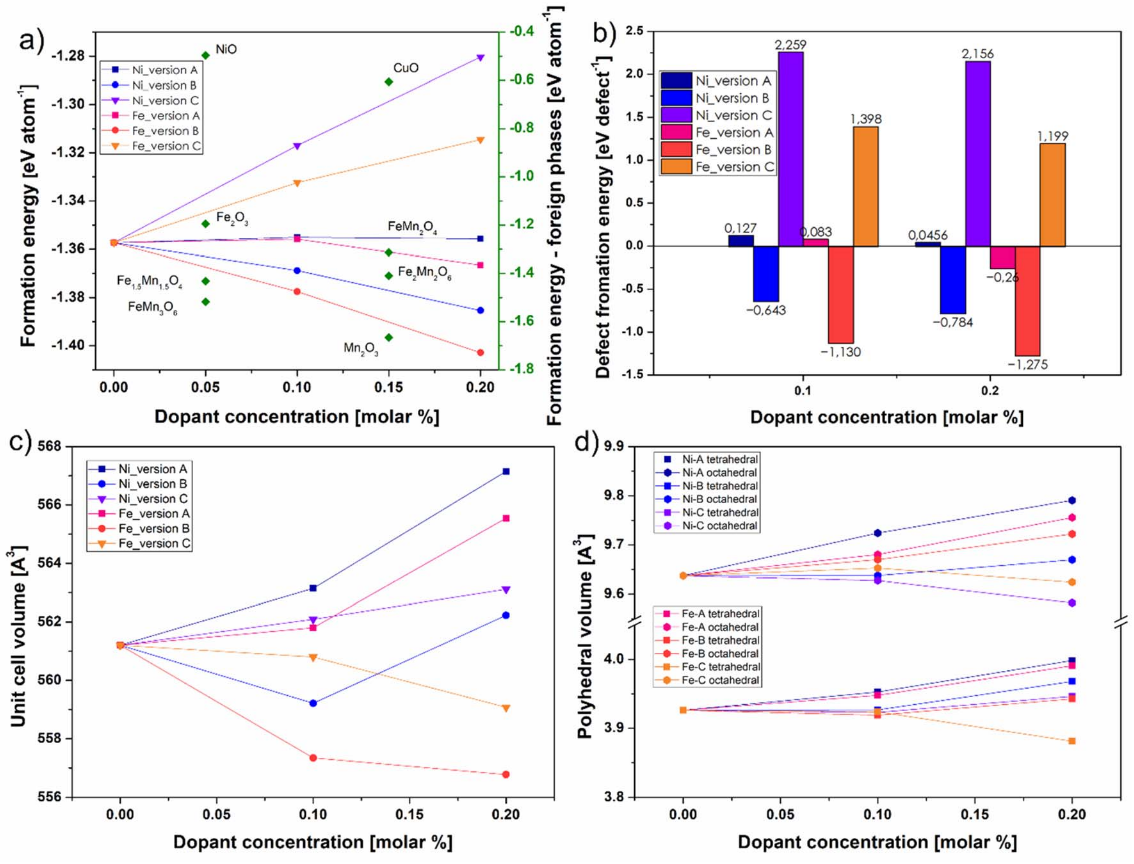

Fig. 4 The formation energy (a) and defect formation energy (b) values of Ni- and Fe-doped $Cu_{1.25}Mn_{1.75}O_4$, unit cell parameters of the Ni- and Fe-doped (c) and the changes in the polyhedral volume of the basic Cu and Mn polyhedra (d).

unlikely, this effect is rather negligible. Therefore, it seems that the incorporation of nickel into this structure should result in an increase in the lattice parameters of the system or, possibly, a slight decrease – if the concentration of the Ni dopant (in octahedral sites) is low. Iron polyhedra are even smaller than nickel ones (especially in octahedral sites, Fig. 4d and Table S1), to the extent that despite the overall elongation of Cu–O and Mn–O bonds due to doping with iron, the lattice parameters of the entire system decrease. The exception is version A of the Fe-doped system (Fe in the tetrahedral sites), for which lattice parameters increase. This effect should be correlated with strong elongation of the remaining Cu–O bonds in tetrahedral sites (Table S1). Therefore, the incorporation of iron despite unfavorable energetic conditions should bring with it either a decrease in lattice parameters – for Fe in octahedral sites, or an increase – if Fe is located in tetrahedral sites. Such a tendency should be reflected in dependence of the FIR spectra for band ν_4 on the mass of cations in tetrahedral positions. However, due to the very low intensity of the two ν_4 bands corresponding to Fe-doped samples in Fig. 2, it is impossible to determine any shift in these bands beyond doubt.

3.3. Electrical properties

Electrical conduction in copper–manganese spinels is governed by small polaron hopping, primarily between Mn^{3+} and Mn^{4+} cations located in octahedral sites.[9,52] In the $Cu_xMn_{3-x}O_4$ system ($0.9 \leq x \leq 1.3$), Cu^{2+} ions may also participate in this process *via* redox transitions involving Mn^{3+}, according to the reaction:

$$Cu^{2+} + Mn^{3+} \rightleftharpoons Cu^{+} + Mn^{4+} \tag{8}$$

This mechanism is facilitated by a high Cu content, which promotes Cu^{2+} incorporation into octahedral sites, thereby increasing the Mn^{3+}/Mn^{4+} ratio and reducing the average distance between hopping sites.[53,54]

The impact of Ni and Fe dopants on the electrical conductivity was evaluated by measuring the temperature-dependent resistance over the 300–875 °C range. The corresponding conductivity curves are presented in Fig. 5a, with Arrhenius-type behavior shown in Fig. 5b. All conductivity values were corrected for sample porosity (Fig S2) using eqn (4).

The data indicate that CM01Ni, CM03Ni, and CM01Fe spinels, as in the case of pure CM, exhibited conductivity maxima within distinct temperature ranges, highlighting the role of Ni and Fe dopants in shaping electrical behavior. The undoped CM sample reached a maximum conductivity of 183 S cm^{-1} at ~675 °C, while higher values were observed for doped samples: CM01Ni (192 S cm^{-1} at ~700 °C), CM03Ni (199 S cm^{-1} at ~775 °C), and CM01Fe (197 S cm^{-1} at ~725 °C).

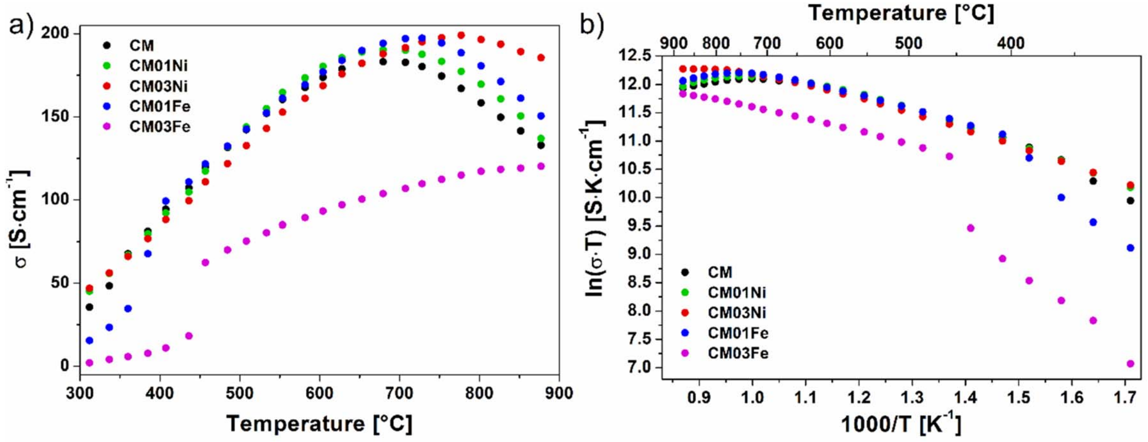

Fig. 5 (a) Temperature dependence of electrical conductivity and (b) Arrhenius plot for Ni or Fe doped CM sinters and a reference CM sinter.

Increasing Ni content to 0.3 mol not only enhanced conductivity but also improved its stability at elevated temperatures, making CM03Ni particularly promising for high-temperature SOEC/SOFC applications. This performance was consistent with structural studies, which confirmed that Ni-doped spinels retain a single-phase structure after sintering (XRD) and exhibit minimal local distortion (FTIR), preserving effective carrier pathways. In contrast, CM03Fe exhibited the lowest conductivity across the entire temperature range and a fully thermally activated transport profile, which correlates with its biphasic composition and increased structural disorder evidenced by FTIR band broadening. For both CM01Fe and CM03Fe, conductivity increased sharply above 400–450 °C, indicating dopant-sensitive transport mechanisms. Below the conductivity maximum, all doped samples exhibited typical semiconducting behavior, with conductivity decreasing at higher temperatures due to reduced polaron mobility.

Table 2 lists the electrical conductivity values of the studied sinters at 650 °C and 800 °C, a temperature range relevant to SOEC/SOFC applications. It also includes activation energy (E_a) values calculated from eqn (5) for temperature ranges where conductivity followed an Arrhenius-like behavior. The analysis indicates that Fe doping reduced E_a compared to pure CM sinter, which may have resulted from increased carrier concentration (Fig S4b, c and Table S2) due to Fe-induced reduction of Mn^{4+} to Mn^{3+}/Mn^{2+}, as seen in the XAS spectra. However, this lower activation energy does not necessarily imply better overall conductivity, particularly in the case of CM03Fe, where the coexistence of multiple phases hindered carrier mobility. Ni doping had a negligible effect on E_a, but did not reduce conductivity due to preserved Mn valence states and structural homogeneity, as confirmed by XRD and FTIR.

The highest electrical conductivity among CM spinels was observed for CM01Ni at 650 °C and CM03Ni at 800 °C, highlighting the potential for optimizing spinel composition for maximum conductivity in the 650–800 °C range. Conversely, CM03Fe exhibited the lowest conductivity at both temperature extremes. Doping with small amounts of Ni or Fe slightly increased conductivity at 650 °C by ~3.4% and ~1.7%, respectively, and at 800 °C by ~6.9% and ~13.8%, compared to pure CM. However, higher Fe content significantly reduced conductivity – by ~46.6% at 650 °C and ~26.4% at 800 °C – due to the presence of a poorly conducting tetragonal phase (~40% by weight).[28] CM03Ni, despite lower conductivity at 650 °C, showed a ~23.9% increase at 800 °C, achieving the highest conductivity of all samples.

3.4. Reactivity studies of $Cu_{1.3}Mn_{1.7}O_4$ spinels doped with Ni or Fe with Cr_2O_3

For all examined samples (Fig. 6), the penetration of Cr into the sinter during exposure at 800 °C was found to be accompanied by the formation of a new layer of spinel phase with the

Table 2 Electrical conductivity of the studied sinters at 650 and 800 °C after correcting for porosity (eqn (4), and Fig. S2) and activation energy (E_a) of electrical conductivity in various temperature ranges

			Activation energy	
Sample	σ at 650 °C [S cm^{-1}]	σ at 800 °C [S cm^{-1}]	Temperature range [°C]	E_a [eV]
CM	174	159	350–675	0.23
CM01Ni	180	170	350–700	0.25
CM03Ni	169	197	350–775	0.23
CM01Fe	177	181	400–725	0.20
CM03Fe	93	117	450–875	0.19

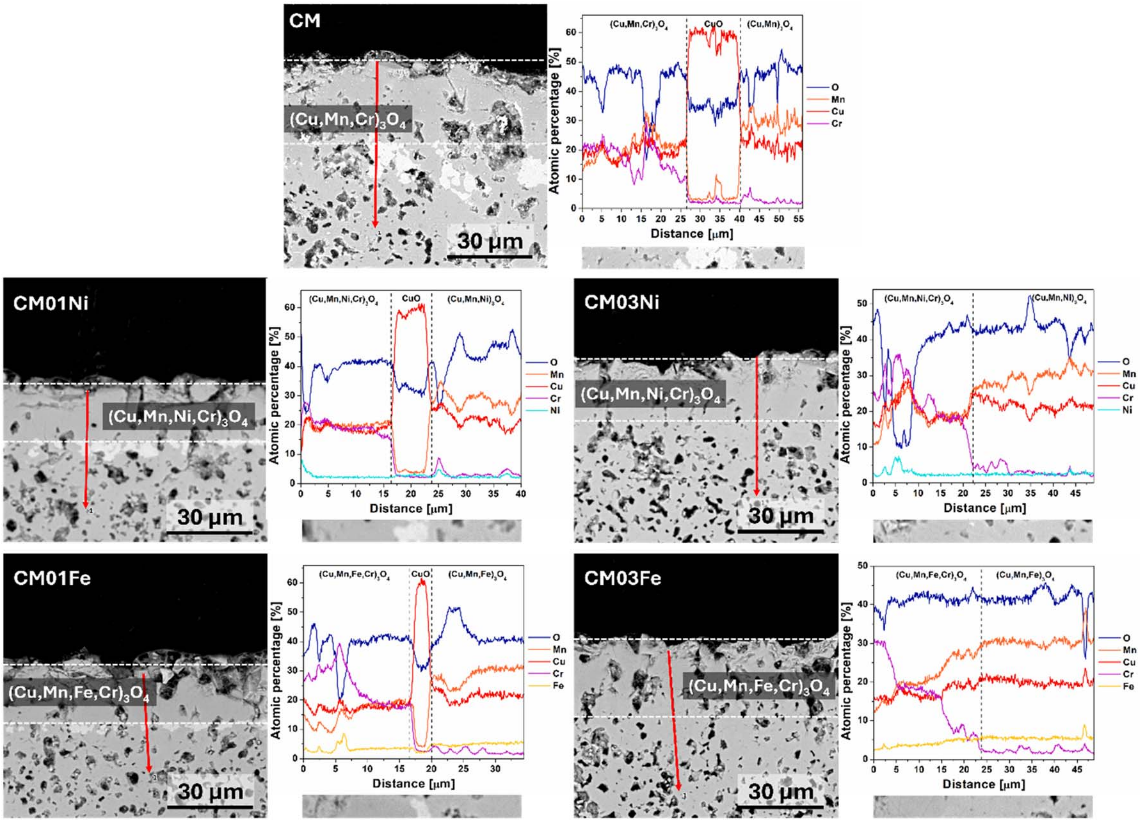

Fig. 6 SEM micrographs of cross-sectional planes of CM01Ni, CM03Ni, CM01Fe and CM03Fe sinters after the reactivity test with Cr_2O_3 involving 150 h in air at 800 °C, and the results of linear EDS analysis of the distribution of Mn, Cu, Cr, Ni, Fe, and O elements along the red line in the SEM micrograph.

composition $(Cu,Mn,(Fe/Ni),Cr)_3O_4$; the thickness of this layer depended on the type of material. For the pure CM sinter, composed of the $(Cr,Cu,Mn)_3O_4$ phase, the thickness of the surface layer was found to be ~26.4 µm, which was larger than for corresponding layers formed on the CM01Ni (~16 µm), CM03Ni (~22 µm), and CM01Fe (~17.5 µm) sinters. On the other hand, the thickest reaction zone with Cr was observed for the CM03Fe sample, with a value of ~25 µm – similar to that observed for pure CM. It is worth adding that segregated copper in the form of CuO, which usually forms at the boundary of the reaction zone with Cr for pure CM sinter, was only observed for samples with a lower dopant content, *i.e.* in CM01Ni (~7 µm) and CM01Fe (~4 µm) samples, and its layer had a thickness of ~12.5 µm. The presence of a continuous CuO layer could block the diffusion of Cr further into the spinel structure. In the case of spinels with a higher Ni or Fe content, the absence of a Cu layer after the reactivity test with Cr_2O_3 can probably be attributed to the significantly lower content of Cu in the composition of these materials. It should be noted that even though the CuO layer blocks Cr diffusion, the presence of a thick and continuous CuO layer may be unfavorable due to the low electrical conductivity (~0.6 S cm^{-1} at 750 °C) of this phase.[55]

The reactivity of spinels with Cr_2O_3 can be explained using crystal field stabilization theory, which predicts ion site preferences based on stabilization energy.[56] Cr^{3+} exhibits the strongest tendency to occupy octahedral sites, preferentially substituting Cu^{2+} rather than Mn^{3+}/Mn^{4+}. In Ni-doped spinels, Ni^{2+} strongly prefers octahedral sites, effectively occupying positions that would otherwise be accessible to incoming Cr^{3+}. As a result, Cr^{3+} has fewer energetically favorable sites to substitute into, which slows down its incorporation and reduces the thickness of the reaction layer. In samples with lower Ni content, CuO formed at the phase boundary due to the incomplete substitution of Cu^{2+} by Ni^{2+}, leading to the preferential exchange of the remaining Cu^{2+} for Cr^{3+}.

For Fe-doped spinels, the behavior was more complex. Fe^{2+}/Fe^{3+} have a lower preference for octahedral coordination than Ni^{2+}, but in the CM01Fe sample, a mechanism similar to what occurs in CM01Ni was observed, with Cr^{3+} substituting residual Cu^{2+} and forming a CuO-rich layer. Unlike Ni, Fe did not integrate fully into the spinel structure at higher concentrations. Instead, it promoted the formation of secondary phases such as tetragonal spinel or bixbyite, leaving more Cu^{2+} ions in the spinel lattice. These remaining Cu^{2+} ions are then readily substituted by Cr^{3+}, which explains the high reactivity observed in CM03Fe.

3.5. Application studies

3.5.1. Oxidation kinetics of coated samples. Fig. 7 presents the oxidation kinetics of ferritic steel coated with CM spinels doped with Ni or Fe ($x = 0.1$ and 0.3), recorded over 3000 h in air

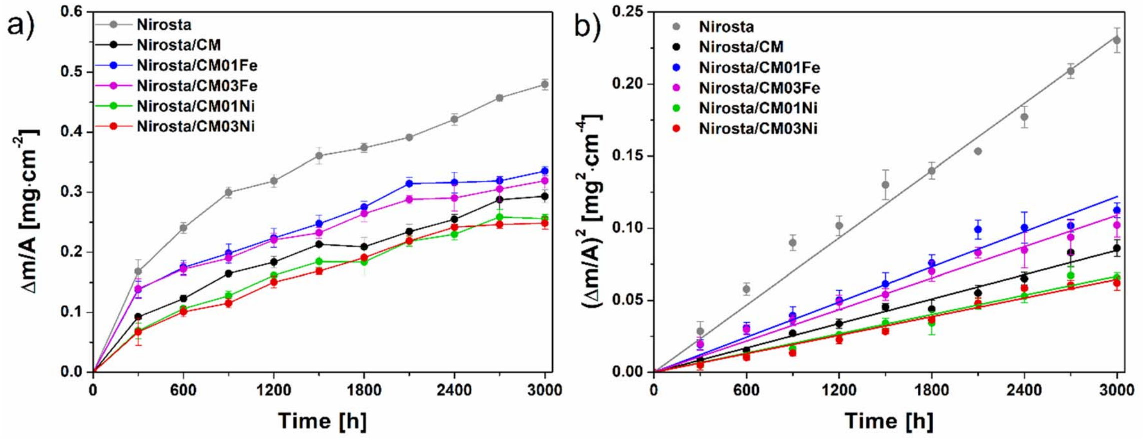

Fig. 7 Oxidation kinetics measured in air at 750 °C over 3000 h for pure Nirosta 4016/1.4016 steel and the same steel with CM spinel coatings doped with Ni or Fe, presented in two coordinate systems: (a) linear and (b) parabolic.

Table 3 Parabolic oxidation rate constants for a series of layered systems with CM spinels doped with Ni or Fe, observed over 3000 h of oxidation in air at 750 °C

Sample	k_p [g^2 cm^{-4} s^{-1}]	R^2
Nirosta	$(2.06 \pm 0.09) \times 10^{-14}$	0.98
Nirosta/CM	$(7.84 \pm 0.18) \times 10^{-15}$	0.99
Nirosta/CM01Fe	$(1.13 \pm 0.03) \times 10^{-14}$	0.99
Nirosta/CM03Fe	$(1.01 \pm 0.03) \times 10^{-14}$	0.99
Nirosta/CM01Ni	$(6.19 \pm 0.16) \times 10^{-15}$	0.99
Nirosta/CM03Ni	$(5.98 \pm 0.19) \times 10^{-15}$	0.99

at 750 °C. Coatings doped with Ni significantly reduce mass gain compared to uncoated steel, while Fe-doped coatings perform worse than undoped CM spinel. The parabolic rate constants (k_p) calculated from the oxidation curves (Fig. 7b) using eqn (7) are collected in Table 3.

Ni-doped coatings reduce the oxidation rate by over 70%, while Fe-doped coatings lower it by ~50%. Compared to undoped CM spinel, doping with Fe increased k_p by ~29%, while doping with Ni reduced it by ~24%. Of the tested systems, CM03Ni exhibited the lowest k_p value, indicating the highest oxidation resistance.

Although differences between samples with 0.1 and 0.3 mol dopant content were modest, the slightly better performance of CM03Ni suggests that a higher Ni content further improves coating compactness and chemical stability. More importantly, the oxidation resistance of the coatings is consistent with the bulk reactivity tests conducted using the Cr_2O_3 powder. Ni-doped spinels exhibited the lowest Cr uptake and the weakest interfacial reactivity, while Fe-doped materials showed clear signs of Cr incorporation and secondary phase formation. This suggests that the intrinsic resistance of the bulk material to Cr attack directly translates to improved long-term performance of the corresponding coatings under oxidative conditions.

The determined parabolic rate constants reflect diffusion-controlled oxidation, and the substantial reduction in k_p for Ni-containing systems highlights their suitability as effective high-temperature corrosion barriers.

3.5.2. Microstructure of sample cross-sections, confocal Raman imaging and high-resolution TEM observations.

SEM cross-sectional images of the layered systems (Fig. 8) show that the thickness of the Ni-doped CM spinel coatings was approximately 34 ± 2 μm – about 15% thicker than the undoped CM spinel coating. In contrast, Fe-doped coatings exhibited a lower thickness of around 25 ± 1 μm. This suggests that, under identical EPD conditions, Fe-doped spinels had inferior deposition behavior or lower suspension stability compared to their Ni-doped counterparts.

CM01Fe and CM03Fe coatings were characterized by large closed pores distributed throughout the entire volume, indicating less compact structure. For CM01Ni and CM03Ni, larger pores were located mainly at the reactive layer/coating interface, with the remaining coating volume exhibiting a low level of closed porosity. These microstructural features may contribute to the observed differences in oxidation resistance.

EDS element distribution maps of chromium reveal a concentration gradient within all tested coatings, originating from the thin intermediate Cr_2O_3-rich layer at the steel interface and extending toward the outer region of the coating. This indicates active diffusion of chromium through the coating. Similar behavior was observed for the undoped CM coating. The element distribution profiles, along with the XRD results (Fig. S5), confirm the absence of CuO in the 0.3 mol Ni-doped coating and the presence of Mn_2O_3 only in the CM03Fe sample; in this case, it was located at the ceramic surface, which supports the observed differences in coating stability and composition.

To precisely determine the phase composition differences between the ferritic stainless steel sample with a pure spinel CM coating (Nirosta/CM) and multilayer systems with Ni-/Fe-doped CM spinel coatings (Nirosta/CM03Ni and Nirosta/CM03Fe) obtained after 3000 h of oxidation in air at 750 °C, their cross-sectional planes were observed using Raman imaging. The results for the aforementioned samples are presented in Fig. 9–

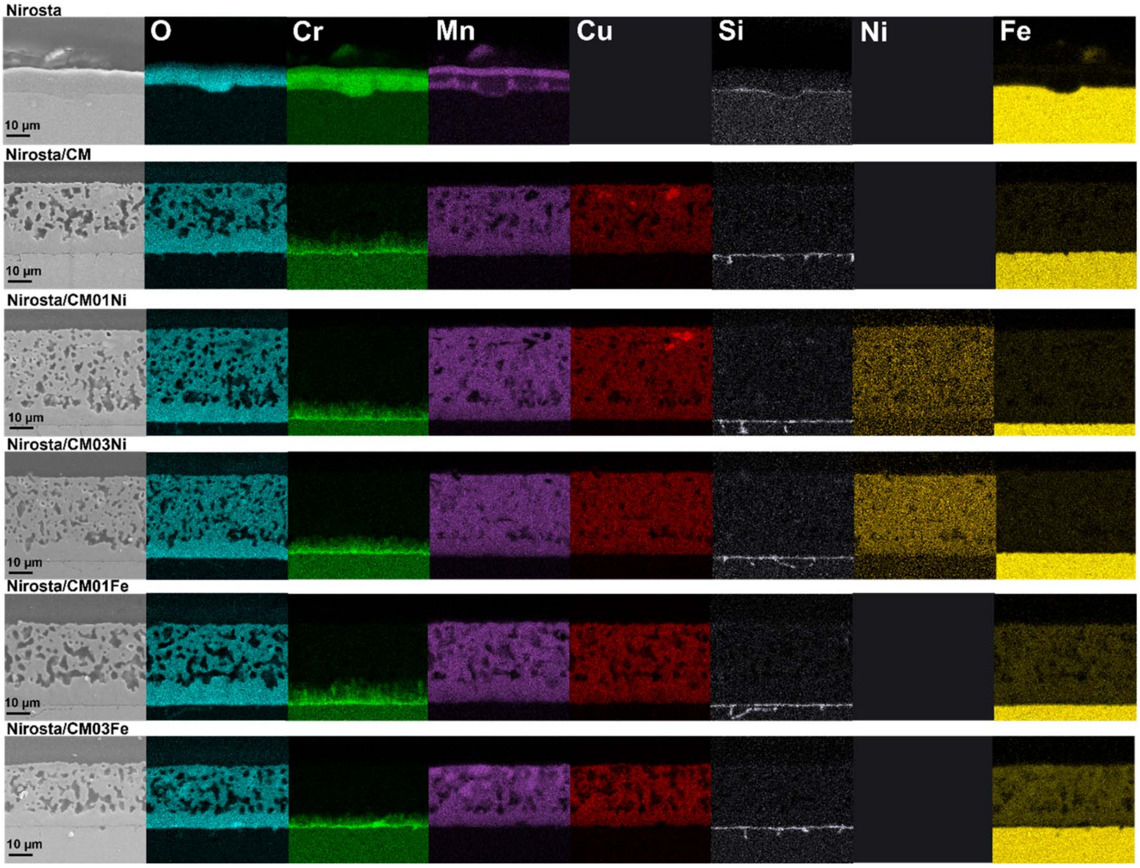

Fig. 8 SEM micrographs of cross-sectional planes of steel/coating layered systems after 3000 h of oxidation in air at 750 °C, and EDS element distribution maps of Cr, Mn, Cu, Si, Ni, Fe and O for all tested samples.

11, with the red rectangle in the confocal image corresponding to the area examined during the measurement.

The distribution images (obtained by integrating the most characteristic band for a given phase) along with the value of the Raman shift used for integration, are presented together with the corresponding Raman spectra from a given area, selected manually. Each spectrum is labeled with bands that can be uniquely assigned to the individual phases in the sample. In some cases, one spectrum was used to integrate two phases (*e.g.* $(Mn,Cr)_3O_4$ and MnO_2). The obtained results complement those of the XRD (Fig. S5) and EDS analyses, providing complete information about the phase composition of individual areas in the coatings and scale. The Raman spectroscopy results in Fig. 9 for the sample with a pure CM spinel coating show that at the interface between the steel substrate and the coating, a thin layer of phases constituting the scale was found.

One of these phases is the $(Mn,Cr)_3O_4$ spinel, which was identified based on the characteristic bands at around 511 and 684 cm^{-1}.[57,58] Its presence in the scale was also confirmed *via* X-ray diffraction studies (Fig. S5) and EDS analysis (Fig. 8). It should be noted that the spinel forms a mixture with a smaller amount of the MnO_2 phase (characteristic bands at 531 and 639 cm^{-1} (ref. 45)), which may not be visible in the XRD patterns due to overly low content that is below the detection level of XRD. Below the layer of manganese-chromium spinel/MnO_2, Raman imaging revealed the presence of a layer consisting of the Cr_2O_3 phase (bands at around 295, 351, and most characteristic ones at 554 and 612 cm^{-1} (ref. 59)), which had been observed in the EDS element distribution map. In addition, the presence of the dense intermediate reaction layer rich in Cr above the layer of these phases was confirmed; the layer, which can be seen in the SEM micrographs, consisted of two spinel phases that differed from one another and – most importantly – from the CM spinel in terms of the ordering of the structure and chromium content. Above this dense layer, the presence of the proper CM coating material was confirmed based on the most characteristic band at around 572 cm^{-1} and bands at around 90, 120, and 426 cm^{-1}.[60,61] The presence of two types of spinels below the pure CM layer, designated as $(Cu,Mn,Cr)_3O_4$-1 and $(Cu,Mn,Cr)_3O_4$-2, was determined based on the characteristic spinel bands, which were shifted relative to the most characteristic band from the CM spinel, and were also significantly broadened.[62] For the $(Cu,Mn,Cr)_3O_4$-1 spinel, which was closer to the metal core, this band occurred at around 501 cm^{-1}, while for $(Cu,Mn,Cr)_3O_4$-2, it was observed at around 532 cm^{-1}. In accordance with the predictions made as part of the EDS analysis, the phase closer to the steel/coating interface should contain more Cr, which manifests in the spectrum as a more pronounced Raman shift.[61] Additionally, the higher chromium content in the $(Cu,Mn,Cr)_3O_4$-1 spinel compared to

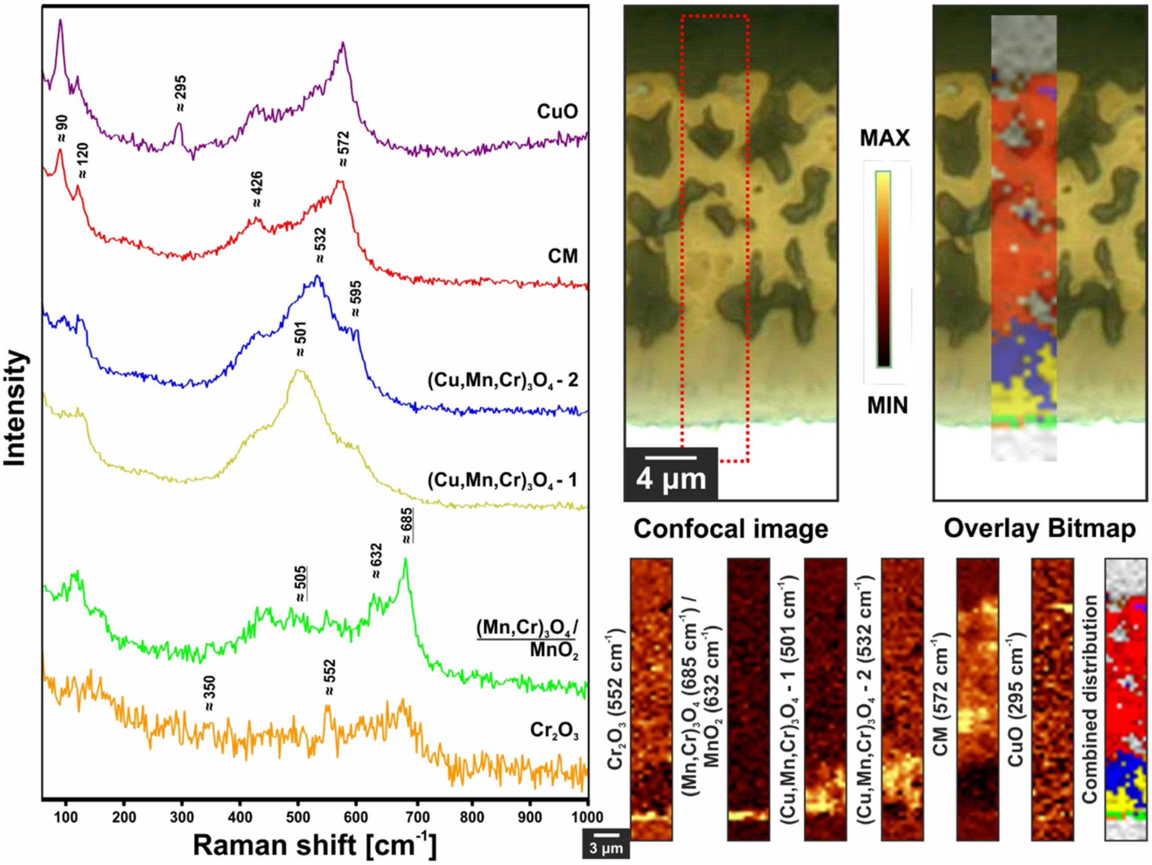

Fig. 9 Raman imaging of a cross-sectional plane of the Nirosta/CM layered system after 3000 h of oxidation in air at 750 °C, showing the distribution of phases along with their Raman spectra.

$(Cu,Mn,Cr)_3O_4$-2 indicates its greater structural disorder, which is reflected in the respective Raman spectrum by the greater broadening of the characteristic bands.[62] Furthermore, Raman imaging confirmed the occurrence of the CuO phase in the upper part of the coating (characteristic band at around 295 cm^{-1} (ref. 63)), which had also been observed in the XRD diffractogram and the Cu distribution map for this sample (Fig. S5 and 8).

Fig. 10 and 11 present the results of Raman imaging for multilayer systems with CM spinel coatings modified with the highest amounts of Ni or Fe dopants – the Nirosta/CM03Ni (Fig. 10) and Nirosta/CM03Fe (Fig. 11), respectively.

For both CM03Ni and CM03Fe, the presence of four phases containing Cr was detected below the phase corresponding to these materials (two phases corresponding to the scale and two in the reaction zone with the coating). Starting from the metallic substrate, the respective phases were: Cr_2O_3 (band at around 555 cm^{-1} (ref. 59)) and $(Mn,Cr)_3O_4$ (band at around 681 cm^{-1} (ref. 57 and 58)) – for the scale, and $(Cu,Mn,Ni/Fe,Cr)_3O_4$-1 (band for Ni dopant at around 508 and Fe at around 509 cm^{-1} (ref. 60 and 61)) and $(Cu,Mn,Ni/Fe,Cr)_3O_4$-2 (band for Ni dopant at around 538 and Fe at around 531 cm^{-1} (ref. 60 and 61)) spinels – for the intermediate reaction layer.

Analogous phases were also detected in the coating based on pure CM spinel (Fig. 9). This means that the mechanism underlying the oxidation of multilayer systems with coatings based on copper–manganese spinel is similar. The difference, however, is in the degree of coating densification and the thickness of the intermediate reaction layer rich in Cr, which had been observed in SEM micrographs (Fig. 8). In addition, the Raman imaging of the tested samples confirmed the results of X-ray diffraction studies (Fig. S5) and the EDS element distribution maps (Fig. 8) for these samples, which indicated the absence of CuO, as was the case for the multilayer system with a coating based on pure CM spinel. Additionally, Fig. 11 shows the presence of significant amounts of the Mn_2O_3 phase for the Nirosta/CM03Fe sample (characteristic bands at around 315 and 692 cm^{-1} (ref. 45)), which is also in agreement with the results of X-ray diffraction studies and EDS chemical composition analyses.

The high-temperature oxidation behavior of the $CuMn_{1.7}Ni_{0.3}O_4$ spinel-coated ferritic stainless steel reveals a complex, chemically graded interface shaped by extensive element interdiffusion processes. This interfacial region was thoroughly analyzed using STEM-EDS element mapping, point analysis, and line scans, as presented in Fig. 12a–c. The transition from the ferritic steel substrate to the spinel coating is marked by a clear composition gradient, with distinct zones of element enrichment and depletion across the interface. A key observation from Fig. 12 is that substantial inward diffusion of

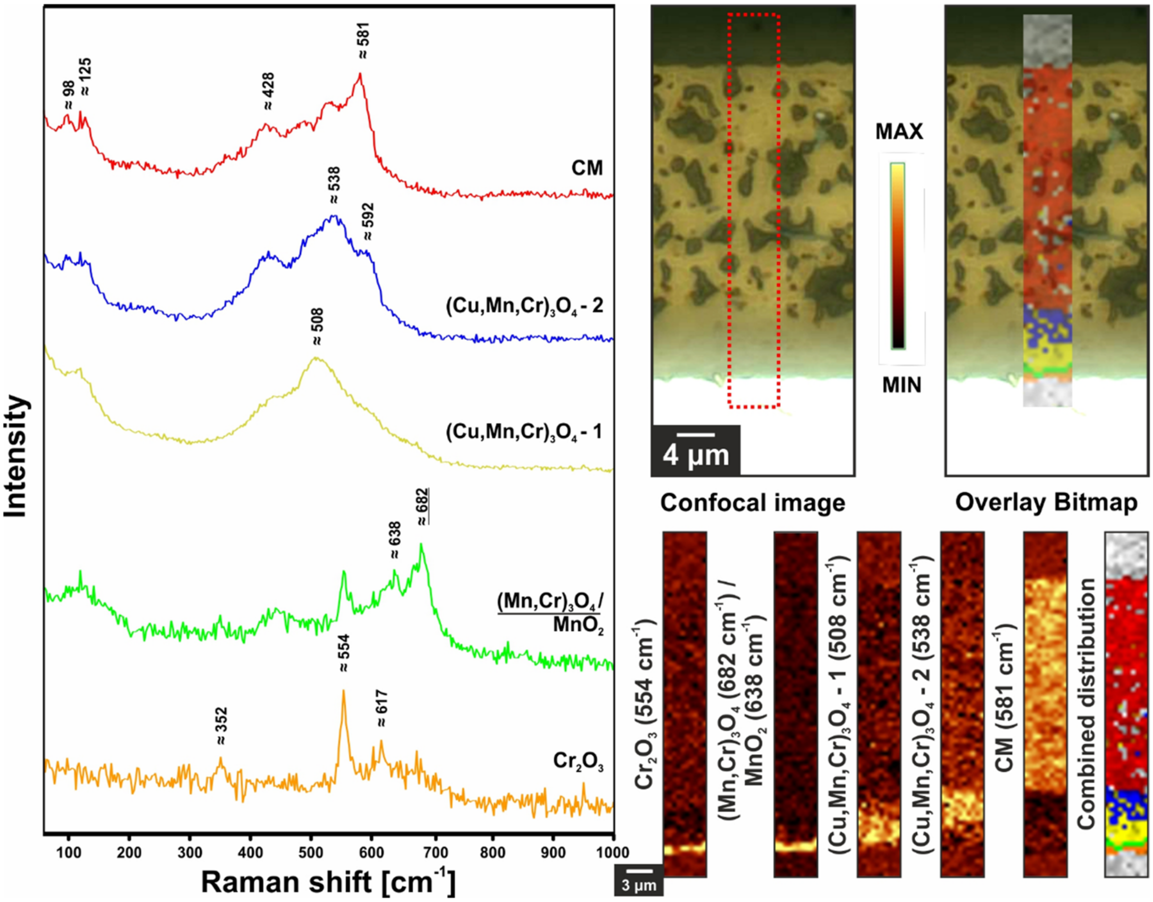

Fig. 10 Raman imaging of a cross-sectional plane of the Nirosta/CM03Ni layered system after 3000 h of oxidation in air at 750 °C, showing the distribution of phases along with their Raman spectra.

chromium from the steel substrate into the spinel layer had occurred, reaching further than for the Co–Mn based spinel coatings.[64] Chromium, initially concentrated in the steel, formed a pronounced Cr-rich oxide at the interface. This is evidenced by a strong Cr signal in the EDS map (Fig. 12a), a distinct peak in the Cr line scan (Fig. 12c), and elevated Cr concentrations (up to ∼35 at%, *e.g.* area 7 in Fig. 12b). The presence of oxygen in this region suggests the formation of a dense Cr_2O_3-type layer typical of selective oxidation processes.

Beyond the immediate interface, chromium continued to migrate several microns into the spinel coating (*e.g.* at areas 4 and 8), altering its local stoichiometry. The element distribution of other cations was also analyzed. Manganese remained distributed throughout the coating, with concentrations increasing toward the outer surface (*e.g.* >20 at% at areas 6 and 9 in Fig. 12b). On the other hand, areas with high chromium concentrations were depleted in manganese. Copper exhibited localized depletion in intermediate zones (*e.g.* areas 1, 2 and 4) especially in the grains for which high concentrations of chromium were observed, whereas nickel had a moderate distribution, again with the exception of areas with considerable chromium accumulation. These distributions indicate cationic redistribution during oxidation and spinel formation, potentially affecting the local electrical and chemical properties of the coating.

Building on this chemical characterization, the high-resolution microstructural analysis shown in Fig. 13a–e provided further insight into the morphology and phase distribution within the interface. The STEM-BF image (Fig. 13a) revealed a multilayered structure. A thin layer closest to the Nirosta steel substrate consisted of amorphous SiO_2, which had originated from the steel. It should be emphasized that this SiO_2-rich interlayer was not continuous, which is important with regard to its electrical properties. Above this amorphous film was a continuous Cr_2O_3 interlayer with a nanocrystalline nature and compact morphology. The existence of this Cr_2O_3 phase confirmed previous STEM-EDS findings and was consistent with the strong chromium diffusion observed across the interface. The spinel coating above this layer exhibited a well-ordered regular structure, confirmed by the observed SAED patterns (Fig. 13b and c) and high-resolution STEM-HAADF imaging (Fig. 13d). The corresponding simulated image (Fig. 13e) was consistent with the experimental data, confirming that the spinel was structurally coherent with the [101] zone axis orientation. When considered together, the data in Fig. 13 confirm that chromium had formed a nanocrystalline oxide

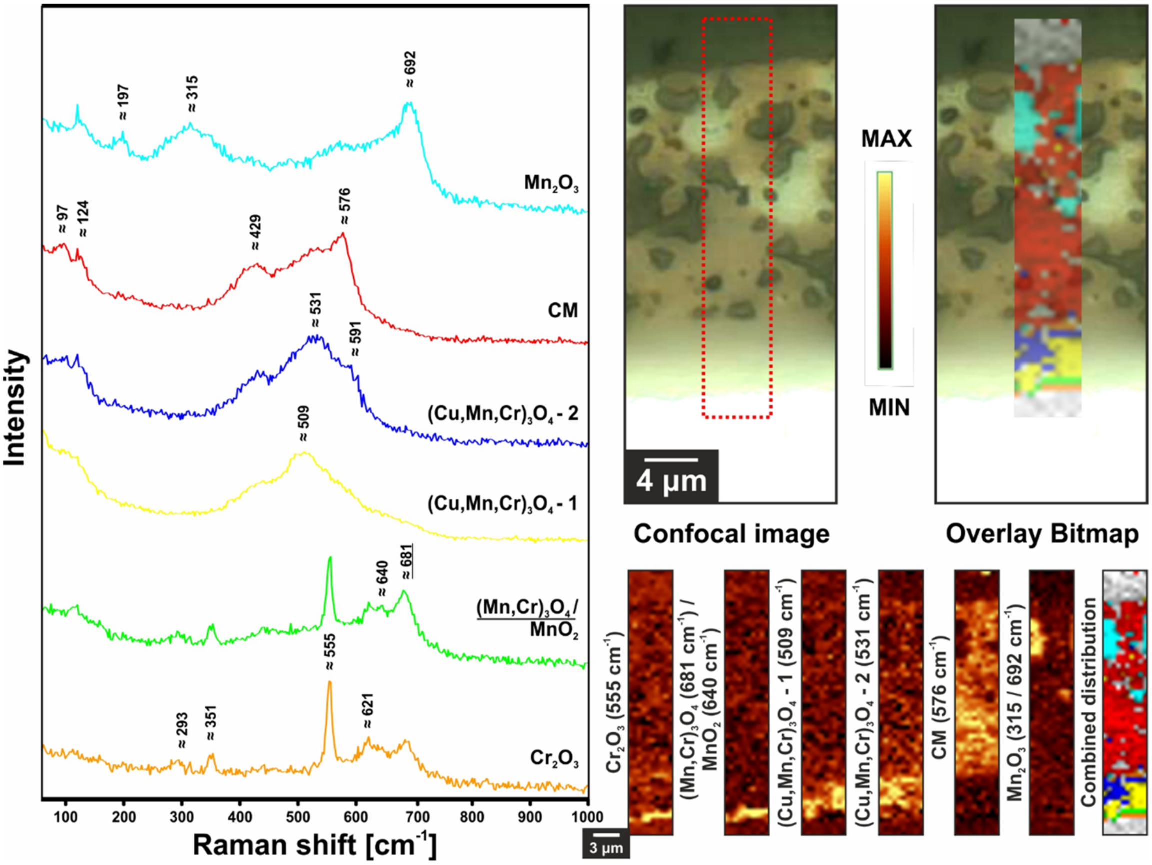

Fig. 11 Raman imaging of a cross-sectional plane of the Nirosta/CM03Fe layered system after 3000 h of oxidation in air at 750 °C, showing the distribution of phases along with their Raman spectra.

layer at the interface and had simultaneously diffused into the spinel coating, modifying its chemistry without disrupting structural continuity.

To gain a broader understanding of the coating's structural integrity, Fig. 14a–d provides a comprehensive cross-sectional analysis of the oxide layer, combining imaging, diffraction, and chemical techniques. The STEM-HAADF image (Fig. 14a) identified three distinct regions. Region 1, located closest to the steel substrate, corresponds to a compact, fine-grained Cr_2O_3 layer. The EDS point analysis in this region revealed a high chromium content, confirming earlier observations of selective oxidation and Cr enrichment at the metal/oxide interface. However, a notable anomaly in this dataset is the elevated copper signal (53.5 at%), which likely originated from the copper-based sample holder rather than the specimen itself, as this area on the lamella had come into contact with the holder during measurements.

Moving away from the steel interface, region 2 displays a complex oxide zone enriched in Cr and Cu, with an intermediate concentration of Mn. This composition suggests a transitional zone between the Cr_2O_3 interlayer and the outer spinel phase, possibly reflecting the onset of Cr incorporation into the spinel lattice. The presence of small spinel grains is consistent with this compositionally graded transition, further supporting the notion of progressive chromium diffusion during high-temperature exposure. Region 3, which was located in the porous outer part of the coating, is characterized by a composition dominated by Mn and Cu, with reduced Cr content. The corresponding HAADF images (Fig. 14b) reveal well-defined crystalline grains in all three regions. SAED patterns collected for all three regions (Fig. 14c) match known spinel reflections, confirming phase identity and structural continuity despite local chemical variations. Finally, HRSTEM-HAADF imaging (Fig. 14d) and digitally filtered insets show high crystallinity across all regions, with well-resolved lattice fringes and atomic columns. This structural coherence suggests that the spinel coating remains robust under thermal stress, even as element diffusion occurs.

3.5.3. Area-specific resistance of steel/coating systems. Area-specific resistance (ASR) measurements (Fig. 15) revealed that layered systems with Ni-doped CM spinel coatings consistently achieved ASR values below the critical 100 mΩ cm^2 threshold for SOEC/SOFC interconnects at temperatures above 500 °C. In contrast, systems with Fe-doped CM coatings reached this threshold only above 550 °C. Notably, doping with Ni led to a significant reduction in ASR across the entire temperature range, especially at lower temperatures, while doping with Fe increased resistance values compared to undoped CM coatings.

All ASR measurements were conducted after 3000 h of oxidation in air at 750 °C, highlighting the long-term electrical a)

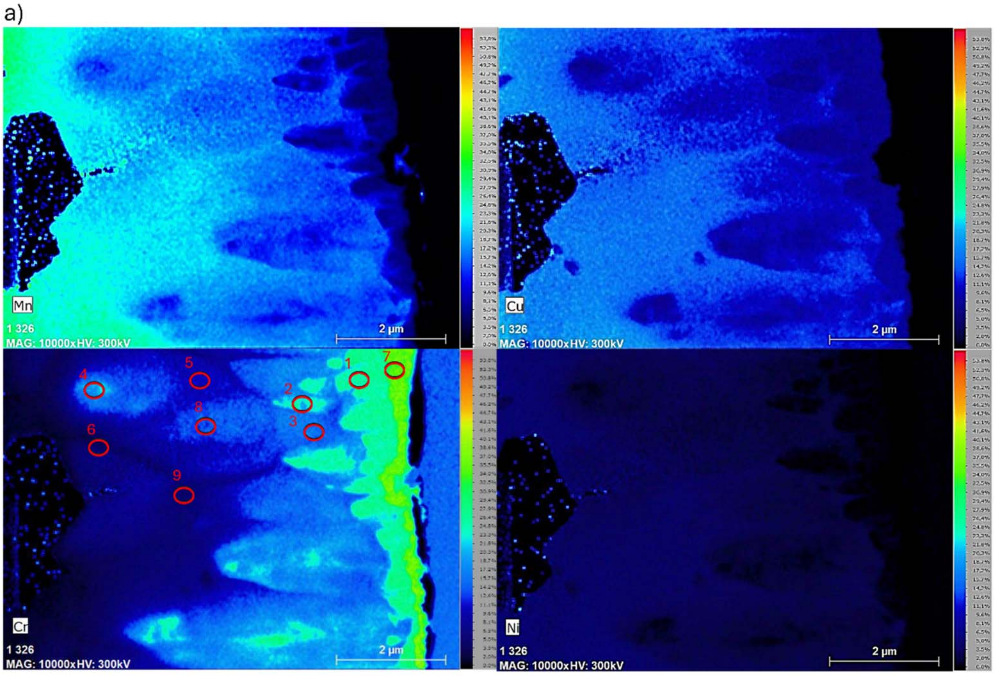

b)

	Atomic %					
Position	Fe	Cr	O	Cu	Ni	Mn
1	0.3	25.3	60.1	7.6	0.6	5.9
2	0.4	23.5	59.5	7.2	0.7	8.5
3	0.5	15.8	57.9	9.9	2.0	13.7
4	0.5	18.9	57.2	7.9	1.3	14.0
5	0.6	10.4	56.3	12.3	2.9	17.3
6	0.6	4.3	53.9	15.4	3.9	21.8
7	0.2	34.7	64.2	0.2	0.1	0.5
8	0.5	13.6	58.7	9.8	2.2	15.0
9	0.6	4.9	53.2	15.5	4.2	21.4

c)

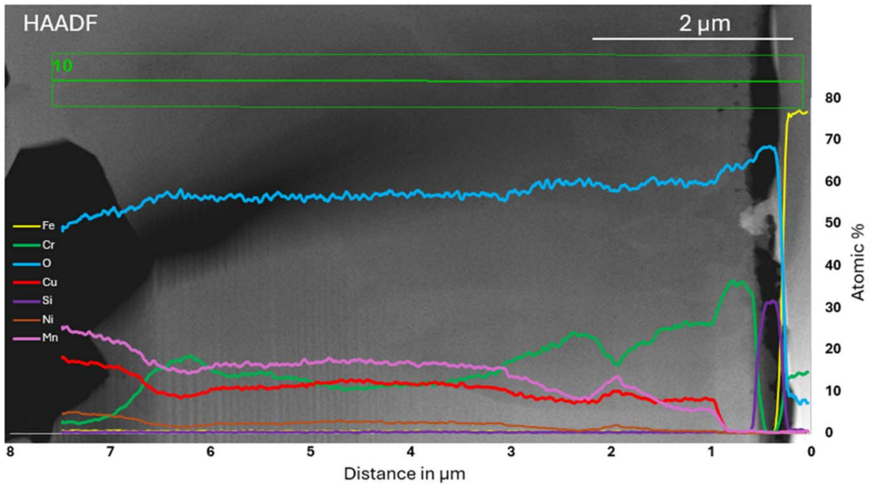

Fig. 12 Chemical composition analyses (STEM-EDS) of the region adjacent to the metallic substrate: (a) quantitative distribution map in the analyzed region, (b) results of quantitative chemical composition analyses in areas marked in (a and c) line profile of the distribution of selected elements, quantitative analysis.

stability of the coatings. At the threshold operating temperature of 750 °C, the lowest ASR values were obtained for CM03Ni (14.6 ± 0.1 mΩ cm^2) and CM01Ni (15.4 ± 0.1 mΩ cm^2), with both materials slightly outperforming the undoped CM coating (16.5 ± 0.1 mΩ cm^2). In contrast, Fe-doped coatings showed significantly higher resistance, with ASR values of 18.1 ± 0.2 mΩ cm^2 (CM01Fe) and 19.7 ± 0.3 mΩ cm^2 (CM03Fe). The progressive increase in ASR with Fe content suggests that electronic

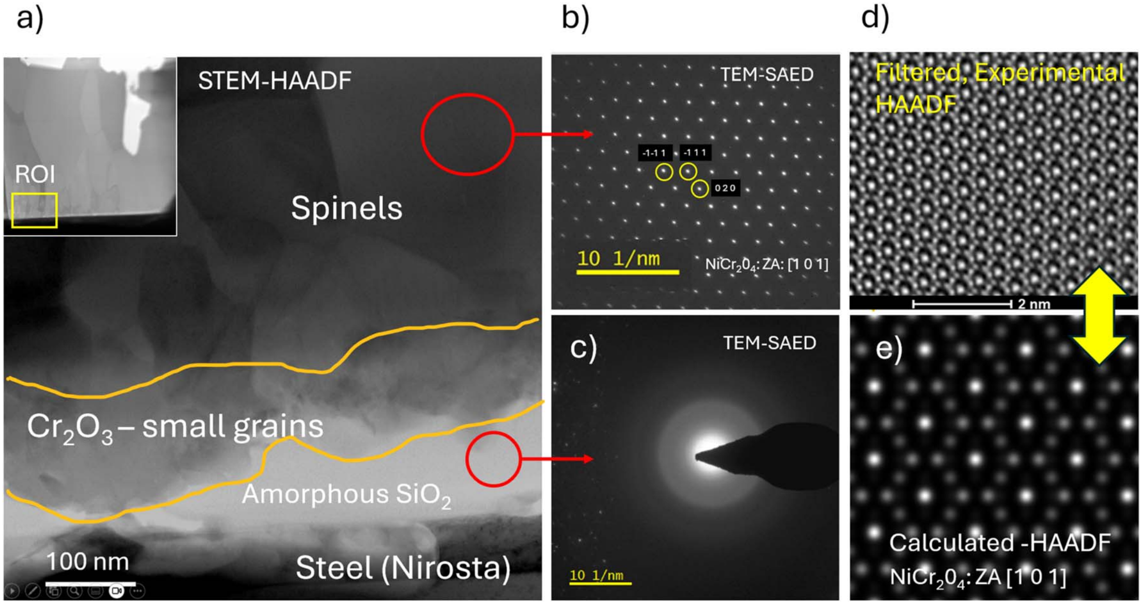

Fig. 13 Results of microstructural analyses of selected areas located in the layer deposited/formed on steel: (a) STEM-BF image of the area is marked with a yellow rectangle in the inset, which shows the lamella at low magnification; an amorphous SiO_2 layer adjacent to the Nirosta steel substrate is highlighted, followed by a fine-crystalline Cr_2O_3 layer, and spinel crystallites above it, (b) TEM-SAED diffraction patterns recorded for the spinel and SiO_2 regions, (c and d) acquired and digitally filtered HRSTEM-HAADF images of $NiCr_2O_4$ spinel with [101] zone axis orientation and (e) simulated HAADF image of this spinel.

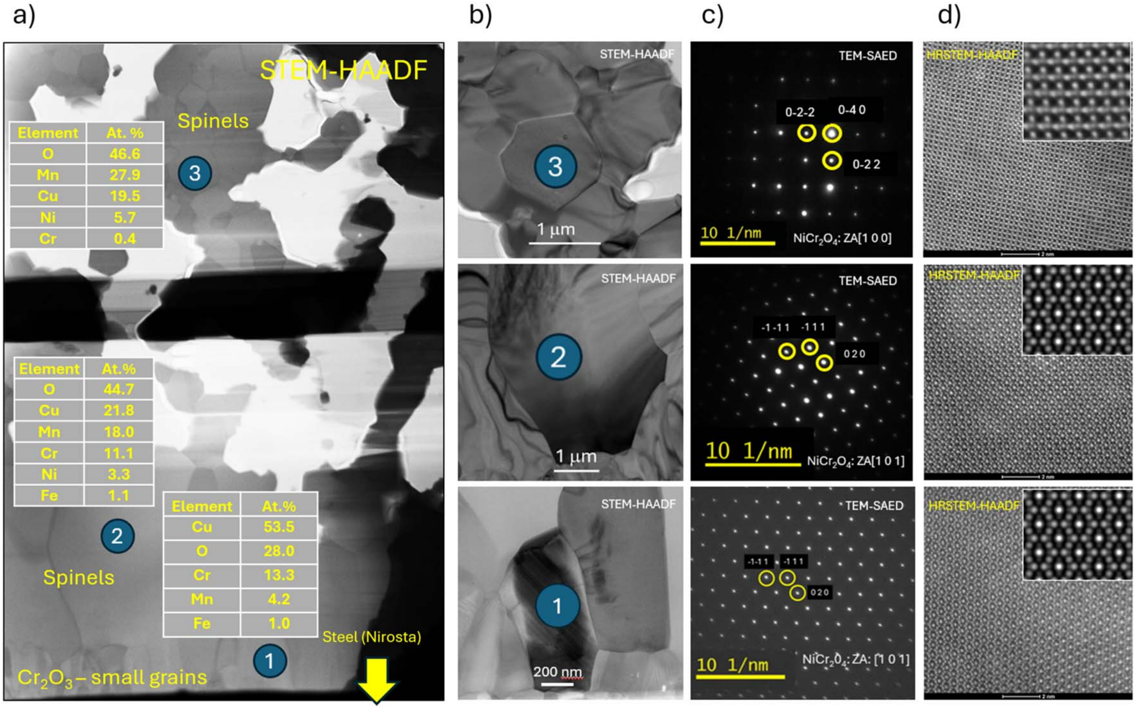

Element	At. %
O	46.6
Mn	27.9
Cu	19.5
Ni	5.7
Cr	0.4

Element	At.%
O	44.7
Cu	21.8
Mn	18.0
Cr	11.1
Ni	3.3
Fe	1.1

Element	At.%
Cu	53.5
O	28.0
Cr	13.3
Mn	4.2
Fe	1.0

Fig. 14 Microstructure across the substrate/scale boundary layer, the spinel region and the area with high porosity (STEM-HAADF). Results of TEM-SAED diffraction analyses and HRSTEM-HAADF images of selected areas of the sample, (a) chemical composition in the areas marked 1–3; (b) HAADF images of sites for which diffraction analyses (TEM-SAED) and high-resolution imaging (HRSTEM-HAADF) had been performed, (c) diffraction images with solutions, (d) HRSTEM-HAADF images of selected areas with magnified and digitally filtered fragments of the HAADF image (insets).

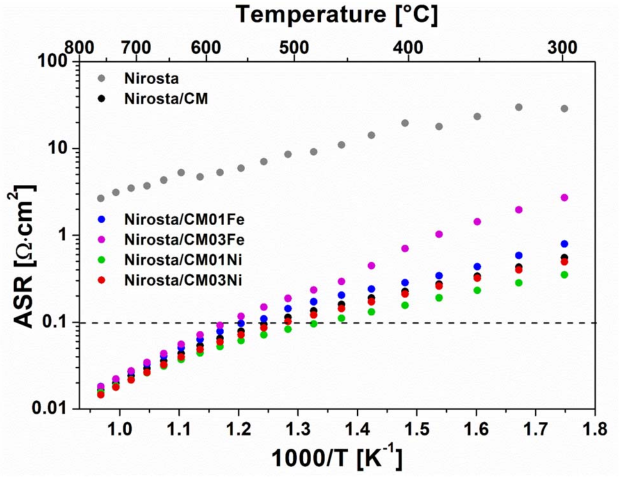

Fig. 15 Arrhenius plot of area-specific resistance (ASR) as a function of temperature for layered systems which had been oxidized for 3000 h in air at 750 °C.

transport degrades for higher dopant levels, which is likely associated of structural disorder and the presence of poorly conducting Mn_2O_3,[65] as confirmed by Raman and XRD analyses.

The minimal difference between CM01Ni and CM03Ni indicates that even small additions of Ni are sufficient to stabilize the spinel structure, enhance phase homogeneity, and suppress the formation of detrimental secondary phases. These electrical trends are highly consistent with oxidation kinetics data and microstructural observations – particularly the improved coating density, reduced porosity, and chemically coherent interfaces in Ni-doped systems. This highlights the potential of Ni-doped CM spinels as promising candidates for stable, low-resistance, Co-free interconnect coatings in electrochemical devices operating at high temperatures.

4. Discussion

The structural distinctions introduced by Ni and Fe doping not only influenced phase stability and crystallographic order but also had a profound impact on the electronic transport and chemical reactivity of CM-based spinels. Electrical conductivity measurements revealed that the preservation of a single-phase spinel structure with minimal local distortion in Ni-doped samples directly translated to enhanced charge transport *via* small polaron hopping. This effect was most pronounced in CM03Ni, which exhibited the highest conductivity at 800 °C (199 S cm^{-1}), correlating with its structurally ordered lattice (XRD, FTIR) and stable Mn^{3+}/Mn^{4+} redox pairings (XAS). Density functional theory (DFT) calculations supported these observations, confirming that both Ni^{2+} and Fe^{2+} preferentially substitute Cu^{2+} in octahedral positions, with Ni incorporation being energetically more favorable and less disruptive to the crystal lattice. The DFT-derived formation energies also revealed that Fe doping beyond a certain threshold leads to thermodynamically stable secondary phases, explaining the experimentally observed phase separation in CM03Fe. These features for Ni-doped spinels ensured a well-connected network of hopping sites and stable conduction pathways even at elevated temperatures, a desirable trait for high-temperature SOFC/SOEC applications. In contrast, Fe doping—especially at higher levels—led to the formation of secondary phases (*e.g.*, tetragonal spinel), broadened vibrational bands (FTIR), and altered Mn valence states (XAS), all of which disrupted the conduction mechanism. Although CM03Fe showed a higher carrier concentration, attributed to increased Mn^{2+}/Mn^{3+} and Cu^{+} content, its poor structural integrity drastically reduced carrier mobility, making it the least conductive among the samples.

Ignaczak *et al.*[28] demonstrated that Fe-doping influences the electrical conductivity of $Cu_{1.3}Mn_{1.7}O_4$ spinel. For the undoped sample, the conductivity at 800 °C was 130 S cm^{-1}, while for $Cu_{1.2}Mn_{1.7}Fe_{0.1}O_4$ and $CuMn_{1.7}Fe_{0.3}O_4$ doped samples it increased to ~150 and ~140 S cm^{-1}, respectively. However, further addition of iron ($Cu_{0.8}Mn_{1.7}Fe_{0.5}O_4$) drastically reduced the conductivity to approximately 45 S cm^{-1}, which was attributed to the increasing content of the tetragonal spinel phase. As the dopant content increases to 0.1 mol, the conductivity maximum also shifts towards higher temperatures. However, starting from an iron content of 0.3 mol, the conductivity maximum is not observed, and its continuous increase moreover, a sharp increase in electrical conductivity around 400–500 °C was observed, which was linked to dopant-sensitive transport mechanisms; a similar behaviour is also observed in presented study. In the context of thermal stability, in the cited work, the undoped spinel and the one containing 0.1 mole Fe contained cubic spinel and a small amount of CuO. In the cases of 0.3 and 0.5 moles of Fe, both cubic and teragonal spinel were observed.

In another study, $CuMn_2O_4$ was doped with iron.[24] At 800 °C, the undoped spinel exhibited the highest conductivity of approximately 110 S cm^{-1}, while $CuMn_{1.9}Fe_{0.1}O_4$ and $CuMn_{1.7}Fe_{0.3}O_4$ spinels showed conductivities of 90 and 105 S cm^{-1}, respectively. This indicates that different stoichiometries of Cu–Mn spinels respond differently to iron doping, and that their conductivities remain significantly lower compared to $Cu_{1.3}Mn_{1.7}O_4$ spinel investigated in presented work. Both studies demonstrate that increasing Fe content leads to the formation of the tetragonal phase, however for the Fe-doped $CuMn_2O_4$ spinel, $Mn_2O_3/(Mn,Fe)_2O_3$ secondary phases occur.

Zhu *et al.*[27,66] showed that Ni-doping enhances the conductivity of $CuMn_2O_4$ spinel, increasing it from approximately 75 S cm^{-1} (undoped) to 100 S cm^{-1} ($CuNi_{0.2}Mn_{1.8}O_4$) at 800 °C. On the other hand higher Ni content was not so efficient in terms of increasing electrical conductivity (~82 S cm^{-1} for $CuNi_{0.4}Mn_{1.6}O_4$ and ~95 S cm^{-1} for $CuNi_{0.6}Mn_{1.4}O_4$). XRD results indicated that Ni-doping stabilizes the Cu–Mn spinel composition and expands the single-phase spinel region of the phase diagram, with Mn_3O_4 peaks mainly visible in the undoped sample. This finding supports Joshi *et al.*,[30] which reports that conductivity increases upon Ni-doping, from 60 S cm^{-1} for $Cu_{1.18}Mn_{1.82}O_4$ to 115 S cm^{-1} for $Cu_{0.77}Ni_{0.45}Mn_{1.78}O_4$ at 800 °C.

Mazur *et al.*[67] evaluated Ni and Fe-doped $Cu_{1.3}Mn_{1.7}O_4$ spinel but with different doping strategy (equimolar substitution for

Cu and Mn). In this study, the reported electrical conductivities at 800 °C were at the level of ~137 S cm^{-1} for undoped spinel; ~128 and 150 S cm^{-1} for $Cu_{1.25}Mn_{1.65}Ni_{0.1}O_4$ and $Cu_{1.15}Mn_{1.65}Ni_{0.3}O_4$; ~140 and ~106 S cm^{-1} for $Cu_{1.25}Mn_{1.65}Fe_{0.1}O_4$ and $Cu_{1.15}Mn_{1.55}Fe_{0.3}O_4$ spinels. All these compositions contained a secondary phase in the form of CuO. Additionally, spinel with an admixture of 0.3 mol showed the presence of a tetragonal phase. Literature reports consistent trends regarding Fe and Ni doping in various Cu–Mn spinel compositions. However, $Cu_{1.3}Mn_{1.7}O_4$ spinel remains largely unexplored, and this comprehensive study demonstrates that it may exhibit significantly higher electrical conductivity and high phase stability in the desired working temperature range compared to previously reported Cu–Mn ratios.

Furthermore, the interplay between dopant incorporation and reactivity with Cr_2O_3 highlights another critical dimension of dopant-driven structural tuning. Ni doping significantly suppressed Cr diffusion and reaction layer growth, particularly in CM01Ni and CM03Ni, which formed the thinnest Cr-containing spinel layers. This behavior can be attributed to the strong octahedral site preference of Ni^{2+}, which precludes Cr^{3+} substitution by occupying energetically favorable lattice sites, thus hindering Cr penetration. The absence of segregated CuO layers in high-Ni samples further suggests a more complete incorporation of Ni into the spinel lattice and less residual Cu^{2+} available for Cr^{3+} exchange. In contrast, Fe-doped spinels, particularly CM03Fe, exhibited extensive reaction with Cr_2O_3, producing thick Cr-enriched layers (CM03Fe). This outcome is consistent with structural analyses indicating incomplete Fe substitution at greater concentrations, greater phase separation, and residual Cu^{2+} content in the spinel lattice—features that collectively facilitate Cr^{3+} incorporation. Notably, the formation of a CuO-rich interfacial layer in low-doped CM01Ni and CM01Fe samples may partially inhibit Cr diffusion, but its low conductivity renders it undesirable for applications where low resistivity is crucial. The observed correlation between dopant distribution, phase composition, and reactivity with Cr—especially the dopant-specific blocking of Cr^{3+} sites—is a novel mechanistic insight that reinforces the role of tailored cation substitution in tuning not only electrical but also chemical stability in functional spinel oxides.

Building upon the structural insights previously discussed, the application-oriented investigations of the steel/CM spinel systems demonstrate how the dopant-driven modifications in the bulk spinel structure manifest in the performance of coatings under long-term oxidative exposure. Oxidation kinetics data reveal that Ni incorporation significantly enhances the protective capability of the spinel coating, reducing the parabolic oxidation rate constant (k_p) by over 70% relative to bare steel and outperforming both undoped and Fe-doped counterparts. This enhanced performance is tightly coupled with the preserved spinel phase purity and structural coherence observed in CM03Ni, as confirmed by Raman-confocal imaging and high-resolution TEM analyses. Notably, CM03Ni forms a compact coating layer with minimal closed porosity and a thin Cr_2O_3-rich interfacial zone—features indicative of limited Cr diffusion and strong chemical stability at the interface, aligning with the Cr-blocking mechanism proposed from structural, DFT and reactivity studies.

In contrast, Fe-doped coatings, particularly CM03Fe, exhibit pronounced microstructural degradation, including increased porosity and the formation of secondary phases such as Mn_2O_3—confirmed through Raman imaging and SEM-EDS. The formation of secondary phases, particularly visible in Raman-confocal imaging suggests that Fe doping especially at higher concentrations facilitates a less controlled oxidation process with deeper Cr penetration and lower phase stability. While Cr incorporation and formation of reaction zone consisted of $(Cu,Mn,Cr,Ni/Fe)_3O_4$ spinels occurs in all coatings, its extent and effect are notably mitigated in Ni-rich systems, where the Ni^{2+} preference for octahedral sites helps stabilize the lattice and suppress secondary phases segregation—an effect absent in Fe-doped counterparts especially at higher concentrations. This translates to better corrosion resistance of steel/coating systems.

Crucially, area-specific resistance (ASR) measurements provide a direct link between these microstructural differences and the electrical functionality of the coatings. Ni-doped systems consistently demonstrate the lowest ASR values after 3000 h at 750 °C, remaining below the critical 100 mΩ cm^2 threshold across the full operational temperature range. The exceptional performance of CM03Ni (14.6 mΩ cm^2) reflects not only superior electronic transport—enabled by a coherent spinel structure and preserve of Mn^{3+}/Mn^{4+} pairs—but also the maintenance of conductive pathways across the coating-substrate interface. In contrast, Fe-doped samples exhibit higher ASR values, with CM03Fe showing the worst performance, attributable to structural degradation and insulating secondary phases despite high carrier concentrations.

To evaluate the performance of the proposed Ni-/Fe-doped Cu–Mn spinel coatings, a comparison with relevant literature data was provided in Table 4.

Obtained ASR values in this study (14–20 mΩ cm^2 after 3000 h at 750 °C) are among the lowest reported for Co-free Cu–Mn spinel-based coatings. Furthermore, the parabolic oxidation rate constant of 5.98×10^{-15} g^2 cm^{-4} s^{-1} for $CuMn_{1.7}Ni_{0.3}O_4$ on a low chromium (Nirosta 4016/1.4016) steel indicates excellent long-term corrosion resistance, even under severe high-temperature conditions.

While a few systems in the literature may exhibit slightly lower ASR or oxidation rate values, these are often achieved under more favorable conditions—such as shorter oxidation durations, higher temperature at which the measurement was conducted, or the use of more corrosion-resistant steel substrates. Notably, many studies utilize Crofer 22 APU, a high-chromium ferritic stainless steel alloyed with elements such as Ti and La, which significantly enhance its corrosion and electrical properties by promoting the formation of a dense chromia scale and suppressing the development of resistive interlayers. Moreover, steels like Crofer 22 APU typically do not form SiO_2-rich interfacial layers, which are known to be electrically insulating and are commonly observed in low-cost, additive-free steels. In contrast, the present study demonstrates comparable or superior performance despite employing steels that are

Table 4 Comparison of oxidized steel/coating systems from Cu–Mn and Mn–Co systems

Coating composition/steel substrate	Coating deposition method	Thermal treatment	Oxidation conditions	ASR [mΩ cm^2]	Parabolic oxidation rate constant (k_p) [g^2 cm^{-4} s^{-1}]
$Cu_{1.3}Mn_{1.7}O_4$/Nirosta 4016[a]	EPD	1000 °C/8 h/H_2–Ar	750 °C/3000 h	16.5	7.84×10^{-15}
$Cu_{1.2}Mn_{1.7}Ni_{0.1}O_4$/Nirosta 4016[a]				15.4	6.19×10^{-15}
$CuMn_{1.7}Ni_{0.3}O_4$/Nirosta 4016[a]				14.6	5.98×10^{-15}
$Cu_{1.2}Mn_{1.7}Fe_{0.1}O_4$/Nirosta 4016[a]		850 °C/6 h/air		18.1	1.13×10^{-14}
$CuMn_{1.7}Fe_{0.3}O_4$/Nirosta 4016[a]				19.7	1.01×10^{-14}
$Cu_{1.3}Mn_{1.7}O_4$/Crofer 22 APU[68]	EPD	850 °C/1 h/H_2–Ar 850 °C/100 h/air	800 °C/185 h	6.1	6.25×10^{-14}
$CuMn_2O_4$/Crofer 22 APU[15]	Immersion method	950 °C/2 h/N_2	800 °C/700 h	7	—
$Cu_{1.2}Mn_{1.8}O_4$/Crofer 22 APU[15]		800 °C/2 h/H_2–Ar		11	—
$Cu_{1.4}Mn_{1.6}O_4$Crofer 22 APU[15]				12	—
$Cu_{1.5}Mn_{1.5}O_4$Crofer 22 APU[15]		800 °C/2 h/air		15	—
$CuMn_{1.8}O_4$/Crofer 22 APU[25]	EPD	1000 °C/24 h/H_2–Ar 850 °C/100 h/air	800 °C/500 h	21	—
$Cu_{1.3}Mn_{1.7}O_4$/AISI 430 (ref. 5)	Screen-printing	—	750 °C/500 h	19.3	—
$Cu_{1.4}Mn_{1.6}O_4$/AISI 430 (ref. 69)	EPD	800 °C/3 h/air	750 °C/100 h (cycles)	—	6.68×10^{-13}
		850 °C/3 h/air		—	2.77×10^{-13}
$CuMn_2O_4$/SUS430 (ref. 27)	EPD	950 °C/6 h/H_2–Ar	800 °C/100 h	12	—
$CuNi_{0.2}Mn_{1.8}O_4$/SUS430 (ref. 27)		750 °C/24 h/air		9	—
$Cu_{1.35}Mn_{1.65}O_4$/460FC[70]	EPD	800 °C/3 h/5%H_2–N_2 700 °C/50 h/air	700 °C/1000 h	15 ÷ 29	—
$CuMn_{1.9}Fe_{0.1}O_4$/Crofer 22 APU[24]	EPD	1000 °C/10 h/H_2	750 °C/3000 h	4.5	4.92×10^{-14}
$CuMn_{1.7}Fe_{0.3}O_4$/Crofer 22 APU[24]		800 °C/2 h/air		5.1	4.73×10^{-14}
$CuMn_2O_4$/Crofer 22 APU[24]				5	6.10×10^{-15}
$MnCo_2O_4$/Crofer 22 APU[12]	EPD	900 °C/2 h/H_2–N_2	800 °C/4000 h	13.6	9.00×10^{-15}
$MnCo_{1.7}Cu_{0.3}O_4$/Crofer 22 APU[12]				15.3	1.60×10^{-14}
$MnCo_{1.7}Fe_{0.3}O_4$/Crofer 22 APU[12]		900 °C/2 h/air		15.5	1.30×10^{-14}
$CuMn_{1.8}O_4$/Crofer 22 APU[8]	EPD	1000 °C/24 h/H_2–Ar 850 °C/100 h/air	800 °C/3000 h	26	—
$MnCo_2O_4$/Crofer 22 APU[8]	EPD	1000 °C/1 h/H_2–Ar 800 °C/5 h/air	800 °C/3000 h	55	—
$Mn_{1.2}Co_{1.2}Fe_{0.3}Cu_{0.3}O_4$/Crofer 22 APU[8]	EPD	1000 °C/2 h/H_2–Ar 900 °C/2 h/air	800 °C/3000 h	20.2	—
$Mn_{1.5}Co_{1.5}O_4$/Crofer 22 APU[71,72]	EPD	900 °C/2 h/H_2–Ar 900 °C/2 h/air	750 °C/2000 h	27	1.45×10^{-14}
$Mn_{1.35}Co_{1.35}Fe_{0.3}O_4$/Crofer 22 APU[71,72]	EPD	1000 °C/2 h/H_2–Ar 900 °C/2 h/air	750 °C/2000 h	23	3.30×10^{-15}
$MnCo_2O_4$/Crofer 22 APU[73]	EPD	900 °C/2 h/H_2–Ar 900 °C/4 h/air	800 °C/7000 h	60	6.57×10^{-14}
$MnCo_{1.5}Cu_{0.5}O_4$/SUS430 (ref. 74)	Dip-coating	800 °C/2 h/H_2–Ar 750 °C/2 h/air	750 °C/2000 h	8	2.15×10^{-15}
$Mn_{1.43}Co_{1.43}Cu_{0.15}O_4$/Crofer 22 APU[75]	EPD	900 °C/2 h/H_2–Ar		10.5	8.4×10^{-15}
$Mn_{1.35}Co_{1.35}Cu_{0.3}O_4$/Crofer 22 APU[75]		900 °C/2 h/air	800 °C/1000 h	11.5	7.4×10^{-15}

Table 4 (*Contd.*)

Coating composition/steel substrate	Coating deposition method	Thermal treatment	Oxidation conditions	ASR [mΩ cm^2]	Parabolic oxidation rate constant (k_p) [g^2 cm^{-4} s^{-1}]
$MnCo_2O_4$/SUS431 (ref. 76)	DC magnetron sputtering	850 °C/4 h/air	800 °C/5600 h	10.3	—
$MnCo_{1.94}La_{0.06}O_4$/SUS431 (ref. 76)				7.1	
$MnCo_{1.94}Ce_{0.06}O_4$/SUS431 (ref. 76)				4.6	
$Mn_{1.5}Co_{1.5}O_4$/SUS430 (ref. 77)	EPD	900 °C/2 h/H_2–Ar	800 °C/1000 h	14.5	—
$MnCoCuO_4$/SUS430 (ref. 77)				9.1	
$MnCoFeO_4$/SUS430 (ref. 77)		800 °C/2 h/air		9.5	

[a] This study.

more commercially accessible and exhibit less favorable chemical compositions, making the proposed coating system more broadly applicable from an industrial perspective, regardless of the applied steel substrate.

5. Conclusions

Ni- and Fe-doped $Cu_{1.3}Mn_{1.7}O_4$ spinels were synthesized and evaluated as Co-free protective coatings for ferritic steel interconnects applied in SOEC/SOFC devices. Structural and electronic characterization (XRD, FTIR, XAS) supported by DFT calculations showed that Ni^{2+} preferentially substitutes Cu^{2+} in octahedral sites, leading to lattice expansion, enhanced phase stability, improved electrical conductivity, and reduced reactivity with Cr_2O_3. In contrast, doping with Fe induced secondary phase formation, structural disorder, and Mn^{4+} reduction, adversely affecting both conductivity and chemical resistance.

The study provided a comprehensive structure/property/performance relationship for doped Cu–Mn spinels and fills the gap in research on their long-term behavior as interconnect coatings. Ni-doped spinels – particularly the sample which had been doped with 0.3 mol of Ni – exhibited superior thermal stability and corrosion resistance. Long-term oxidation tests confirmed the durability of all doped coatings, which retained low ASR values (14–20 mΩ cm^2) after 3000 h of oxidation in air at 750 °C. Confocal Raman imaging revealed a homogeneous distribution of the spinel phase in Ni-doped coatings, with minimal CuO segregation, while Fe-doped systems showed inhomogeneous phase composition and local Cu enrichment. TEM analyses of the coating/steel interface confirmed the presence of a thin, nanocrystalline Cr_2O_3 layer and a chemically graded transition zone, especially in Ni-containing coatings, contributing to interfacial coherence and long-term performance.

The results demonstrate that doping with Ni is an effective and scalable strategy for enhancing both the intrinsic material properties and the coating performance in harsh electrochemical environments, advancing the development of Co-free, high-performance interconnect technologies.

Author contributions

Łukasz Mazur: conceptualization, methodology, investigation, project administration, data curation, visualization, writing – original draft, writing – review & editing. Kamil Domaradzki: investigation, methodology, conceptualization, visualization, writing – original draft. Paweł Winiarski: methodology, investigation. Maciej Bik: methodology, investigation, visualisation, writing – original draft. Andrzej Mikuła: visualisation, methodology, investigation, writing – original draft. Juliusz Dąbrowa: conceptualization, methodology. Grzegorz Cempura: investigation, visualisation, methodology. Anna Adamczyk: investigation. Adam Kruk: investigation, visualisation, methodology. Tomasz Brylewski: conceptualization, funding acquisition, project administration, resources, supervision, writing – original draft, writing – review & editing.

Conflicts of interest

There are no conflicts to declare.

Data availability

All data supporting the findings of this study are included in the manuscript and its SI. Additionally, the raw datasets are available from the corresponding authors, upon reasonable request.

Supplementary information includes supplementary results of XRD studies, SEM observations with EDS analysis of sinters, supplementary results of DFT calculations, and studies of the Seebeck coefficient and determination of carrier concentration and activation energy of their mobility. See DOI: https://doi.org/10.1039/d5ta04138d.

Acknowledgements

Funding of National Science Centre (NCN) project No. 2021/41/B/ST8/02187 is gratefully acknowledged (TB).

References

1 J. W. Fergus, *J. Mater. Sci. Eng. A*, 2005, **397**, 271–283.
2 T. Brylewski, T. Maruyama, M. Nanko and K. Przybylski, *J. Therm. Anal. Calorim.*, 1999, **55**, 681–690.
3 T. Brylewski, S. Molin, M. Stygar, M. Bik, P. Jeleń, M. Sitarz, A. Gil, M. Chen and P. V. Hendriksen, *Int. J. Hydrogen Energy*, 2024, **94**, 209–222.
4 J. C. W. Mah, A. Muchtar, M. R. Somalu and M. J. Ghazali, *Int. J. Hydrogen Energy*, 2017, **42**, 9219–9229.
5 N. Hosseini, M. H. Abbasi, F. Karimzadeh and G. M. Choi, *J. Power Sources*, 2015, **273**, 1073–1083.
6 T. Brylewski, A. Kruk, M. Bobruk, A. Adamczyk, J. Partyka and P. Rutkowski, *J. Power Sources*, 2016, **333**, 145–155.
7 J. Beyrami, R. Nogueira Nakashima, A. Nemati and H. Lund Frandsen, *Energy Convers. Manage.:X*, 2024, **23**, 100653.
8 M. J. Reddy, B. Kamecki, B. Talic, E. Zanchi, F. Smeacetto, J. S. Hardy, J. P. Choi, L. Mazur, R. Vaßen, S. N. Basu, T. Brylewski, J. E. Svensson and J. Froitzheim, *J. Power Sources*, 2023, **568**, 232831.
9 M. Rosenberg, P. Nicolau, R. Manaila and P. Pausescu, *J. Phys. Chem. Solids*, 1963, **24**, 1419–1434.
10 S. E. DORRIS and T. O. MASON, *J. Am. Ceram. Soc.*, 1988, **71**, 379–385.
11 B. Talic, H. Falk-Windisch, V. Venkatachalam, P. V. Hendriksen, K. Wiik and H. L. Lein, *J. Power Sources*, 2017, **354**, 57–67.
12 B. Talic, S. Molin, K. Wiik, P. V. Hendriksen and H. L. Lein, *J. Power Sources*, 2017, **372**, 145–156.
13 S. Molin, P. Jasinski, L. Mikkelsen, W. Zhang, M. Chen and P. V. Hendriksen, *J. Power Sources*, 2016, **336**, 408–418.
14 J. Froitzheim, S. Canovic, M. Nikumaa, R. Sachitanand, L. G. Johansson and J. E. Svensson, *J. Power Sources*, 2012, **220**, 217–227.
15 N. S. Waluyo, B. K. Park, S. B. Lee, T. H. Lim, S. J. Park, R. H. Song and J. W. Lee, *J. Solid State Electrochem.*, 2014, **18**, 445–452.
16 X. Chen, P. Y. Hou, C. P. Jacobson, S. J. Visco and L. C. De Jonghe, *Solid State Ionics*, 2005, **176**, 425–433.
17 D. A. Chesson and J. H. Zhu, *J. Electrochem. Soc.*, 2020, **167**, 124515.
18 R. Irankhah, B. Raissi, A. Maghsoudipour, A. Irankhah and S. Ghashghai, *J. Mater. Eng. Perform.*, 2016, **25**, 1515–1525.
19 P. You, X. Zhang, H. Zhang, X. Yang and C. Zeng, *Oxid. Met.*, 2020, **93**, 465–482.
20 S. N. Hosseini, F. Karimzadeh, M. H. Enayati and N. M. Sammes, *Solid State Ionics*, 2016, **289**, 95–105.
21 Y. Pan, Y. Liu, D. Shi, J. Wang, Y. Xie, R. Wang and Z. Xu, *ACS Appl. Energy Mater.*, 2024, **7**, 4950–4959.
22 M. Bobruk, K. Durczak, J. Dąbek and T. Brylewski, *J. Mater. Eng. Perform.*, 2017, **26**, 1598–1604.
23 J. Lemieszek, B. Ignaczak, K. Lankauf, P. Błaszczak, M. Bik, M. Zając, M. Sitarz, P. Jasińskia and S. Molin, *J. Eur. Ceram. Soc.*, 2024, **53**, 116743.
24 J. Ignaczak, L. Zeng, D. F. Sanchez, M. Makowska, K. Górnicka, K. Lankauf, J. Karczewski, P. Jasiński and S. Molin, *Int. J. Hydrogen Energy*, 2023, **48**(92), 36076–36093.
25 Z. Sun, R. Wang, A. Y. Nikiforov, S. Gopalan, U. B. Pal and S. N. Basu, *J. Power Sources*, 2018, **378**, 125–133.
26 Y. Jin, W. Hao, M. Guo, M. Yu, Y. Guo, X. Liu, Z. Yang, B. Ge, Z. Lei, X. Xiong and S. Peng, *Ceram. Int.*, 2023, **49**, 27716–27723.
27 Z. Zhu, C. Darl-Uzu, U. Pal, S. Gopalan, A. M. Hussain, N. Dale, Y. Fukuyama, Y. Miura, Y. Miyoshi and S. Basu, *Int. J. Hydrogen Energy*, 2022, **47**, 36953–36963.
28 J. Ignaczak, Y. Naumovich, K. Górnicka, J. Jamroz, W. Wróbel, J. Karczewski, M. Chen, P. Jasiński and S. Molin, *J. Eur. Ceram. Soc.*, 2020, **40**, 5920–5929.
29 A. Petric and H. Ling, *J. Am. Ceram. Soc.*, 2007, **90**, 1515–1520.
30 S. Joshi and A. Petric, *Int. J. Hydrogen Energy*, 2017, **42**, 5584–5589.
31 A. Navrotsky and O. J. Kleppa, *J. Inorg. Nucl. Chem.*, 1967, **29**, 2701–2714.
32 Ł. Mazur and T. Brylewski, *Metall. Mater. Trans. A*, 2024, **55**, 5100–5113.
33 P. Wei, M. Bieringer, L. M. D. Cranswick and A. Petric, *J. Mater. Sci.*, 2010, **45**, 1056–1064.
34 G. Kerkhoff, *Material Data Sheet, Ferritic corrosion resisting steel*, 2001, pp. 1–4.
35 Ł. Mazur, K. Domaradzki, P. Winiarski, Ł. Zych and T. Brylewski, *Ceram. Int.*, 2024, **50**, 34017–34026.
36 E. Madej, K. Pitala, A. Kozio, M. Sikora, N. Spiridis, T. Sl and D. W. Sl, *Nucl. Instrum. Methods Phys. Res.*, 2021, **492**, 43–48.
37 G. Kresse and J. Furthmüller, *Comput. Mater. Sci.*, 1996, **6**, 15–50.
38 G. Kresse and J. Hafner, *Phys. Rev. B:Condens. Matter Mater. Phys.*, 1993, **47**, 558–561.
39 J. P. Perdew, K. Burke and M. Ernzerhof, *Phys. Rev. Lett.*, 1996, **77**, 3865–3868.
40 K. Momma and F. Izumi, *J. Appl. Crystallogr.*, 2011, **44**, 1272–1276.

41 R. Landauer, *AIP Conf. Proc.*, 2008, **45**, 2–45.

42 S. Mrowec, *An Introduction to the Theory of Metal Oxidation*, National Bureau of Standards and National Science Foundation, Washington, D.C., 1982.

43 J. Preudhomme and P. Tarte, *Spectrochim. Acta, Part A*, 1971, **27**, 1817–1835.

44 D. Basak and J. Ghose, *Spectrochim. Acta, Part A*, 1994, **50**, 713–718.

45 C. M. Julien, M. Massot and C. Poinsignon, *Spectrochim. Acta, Part A*, 2004, **60**, 689–700.

46 Y. Zhou, S. Sun, J. Song, S. Xi, B. Chen, Y. Du, A. C. Fisher, F. Cheng, X. Wang, H. Zhang and Z. J. Xu, *Adv. Mater.*, 2018, **30**, 1–7.

47 Y. Zhou, S. Sun, C. Wei, Y. Sun, P. Xi, Z. Feng and Z. J. Xu, *Adv. Mater.*, 2019, **31**, 1–11.

48 Y. Sun, H. Liao, J. Wang, B. Chen, S. Sun, S. J. H. Ong, S. Xi, C. Diao, Y. Du, J. O. Wang, M. B. H. Breese, S. Li, H. Zhang and Z. J. Xu, *Nat. Catal.*, 2020, **3**, 554–563.

49 D. S. McClure, *J. Phys. Chem. Solids*, 1957, **3**, 311–317.

50 V. Bisogni, S. Catalano, R. J. Green, M. Gibert, R. Scherwitzl, Y. Huang, V. N. Strocov, P. Zubko, S. Balandeh, J. M. Triscone, G. Sawatzky and T. Schmitt, *Nat. Commun.*, 2016, **7**, 1–8.

51 K. Amemiya, K. Sakata and M. Suzuki-Sakamaki, *e-J. Surf. Sci. Nanotechnol.*, 2022, **20**, 135–138.

52 I. Thaheem, D. W. Joh, T. Noh and K. T. Lee, *Int. J. Hydrogen Energy*, 2019, **44**, 4293–4303.

53 N. Hosseini, F. Karimzadeh, M. H. Abbasi and G. M. Choi, *Ceram. Int.*, 2014, **40**, 12219–12226.

54 P. Stallinga, *Adv. Mater.*, 2011, **23**, 3356–3362.

55 Y. K. Jeong and G. M. Choi, *J. Phys. Chem. Solids*, 1996, **57**, 81–84.

56 J. D. Dunitz and L. E. Orgel, *Adv. Inorg. Chem. Radiochem.*, 1960, **2**, 1–60.

57 R. L. Farrow, P. L. Mattern and A. S. Nagelberg, *Appl. Phys. Lett.*, 1980, **36**, 212–214.

58 N. Madern, J. Monnier, R. Baddour-Hadjean, A. Steckmeyer and J. M. Joubert, *Corros. Sci.*, 2018, **132**, 223–233.

59 J. Mougin, T. Le Bihan and G. Lucazeau, *J. Phys. Chem. Solids*, 2001, **62**, 553–563.

60 T. Van Everbroeck, R. G. Ciocarlan, W. Van Hoey, M. Mertens and P. Cool, *Catalysts*, 2020, **10**, 1–20.

61 H. D. Lutz, B. Müller and H. J. Steiner, *J. Solid State Chem.*, 1991, **90**, 54–60.

62 B. D. Hosterman, PhD thesis, University of Nevada, Las Vegas, 2011.

63 J. Kaur, A. Khanna, R. Kumar and R. Chandra, *J. Mater. Sci.:Mater. Electron.*, 2022, **33**, 16154–16166.

64 T. Brylewski, S. Molin, M. Marczyński, Ł. Mazur, K. Domaradzki, O. Kryshtal and A. Gil, *Int. J. Hydrogen Energy*, 2021, **46**, 6775–6791.

65 F. Hong, B. Yue, N. Hirao, Z. Liu and B. Chen, *Sci. Rep.*, 2017, **7**, 1–7.

66 Z. Zhu, Z. Sun, S. Gopalan, U. B. Pal, A. M. Hussain, N. Dale, Y. Furuya and S. N. Basu, *Jom*, 2025, **77**, 719–728.

67 Ł. Mazur, D. Koszelow, M. Zajusz, M. Łapiński, M. Bik, P. Zając, A. Adamczyk, P. Rutkowski, S. Molin and T. Brylewski, *J. Eur. Ceram. Soc.*, 2023, **43**, 5557–5574.

68 Z. Sun, S. Gopalan, U. B. Pal and S. N. Basu, *Surf. Coat. Technol.*, 2017, **323**, 49–57.

69 A. Norouzi, M. Soltanieh and S. Rastegari, *Int. J. Hydrogen Energy*, 2022, **47**, 14346–14360.

70 S. Oh, D. Kim, I. Lee, C. Choi, J. Lee, Y. Heo and J. Lee, *Int. J. Hydrogen Energy*, 2022, 1–10.

71 E. Zanchi, S. Molin, A. G. Sabato, B. Talic, G. Cempura, A. R. Boccaccini and F. Smeacetto, *J. Power Sources*, 2020, **455**, 227910.

72 E. Zanchi, B. Talic, A. G. Sabato, S. Molin, A. R. Boccaccini and F. Smeacetto, *J. Eur. Ceram. Soc.*, 2019, **39**, 3768–3777.

73 Ł. Mazur, J. Ignaczak, M. Bik, S. Molin, M. Sitarz, A. Gil and T. Brylewski, *Int. J. Hydrogen Energy*, 2022, **47**, 6295–6311.

74 J. Xiao, W. Zhang, C. Xiong, B. Chi, J. Pu and L. Jian, *Int. J. Hydrogen Energy*, 2016, **41**, 9611–9618.

75 S. Molin, A. G. Sabato, H. Javed, G. Cempura, A. R. Boccaccini and F. Smeacetto, *Mater. Lett.*, 2018, **218**, 329–333.

76 H. P. Tseng, T. Y. Yung, C. K. Liu, Y. N. Cheng and R. Y. Lee, *Int. J. Hydrogen Energy*, 2020, **45**, 12555–12564.

77 B. Wang, K. Li, J. Liu, T. Zhang, T. Yang and N. Zhang, *Int. J. Hydrogen Energy*, 2024, **61**, 216–225.